AGU PUBLICATIONS

JGR

Journal of Geophysical Research: Oceans

RESEARCH ARTICLE

10.1002/2013JC009258

A modeling study of coastal circulation and landfast ice in the nearshore Beaufort and Chukchi seas using CIOM

Jia Wang[1], Kohei Mizobata[2], Xuezhi Bai[3], Haoguo Hu[3], Meibing Jin[4], Yanling Yu[5], Moto Ikeda[6], Walter Johnson[7], William Perie[8], and Ayumi Fujisaki[3]

[1]NOAA Great Lakes Environmental Research Laboratory, Ann Arbor, Michigan, USA, [2]Department of Ocean Sciences, Tokyo University of Marine Science and Technology, Tokyo, Japan, [3]Cooperative Institute for Limnology and Ecosystems Research, School of Natural Resources and Environment, University of Michigan, Ann Arbor, Michigan, USA, [4]International Arctic Research Center, University of Alaska, Fairbanks, Alaska, USA, [5]Arctic Science Center, University of Washington, Seattle, Washington, USA, [6]Graduate School of Environmental and Earth Sciences, Hokkaido University, Sapporo, Japan, [7]Department of Interior, Herndon, Bureau of Ocean Energy Management, Virginia, USA, [8]Bedford Institute of Oceanography, Dartmouth, Nova Scotia, Canada

Key Points:
- Modeling landfast ice and nearshore processes
- Reveal mesoscale eddies using a model and theory
- Nearshore sea ice responds to both +DA and −DA

Correspondence to:
J. Wang,
Jia.Wang@noaa.gov

Citation:
Wang, J., K. Mizobata, X. Bai, H. Hu, M. Jin, Y. Yu, M. Ikeda, W. Johnson, W. Perie, and A. Fujisaki (2014), A modeling study of coastal circulation and landfast ice in the nearshore Beaufort and Chukchi seas using CIOM, *J. Geophys. Res. Oceans*, *119*, 3285–3312, doi:10.1002/2013JC009258.

Received 5 JUL 2013
Accepted 29 APR 2014
Accepted article online 3 MAY 2014
Published online 4 JUN 2014

Abstract This study investigates sea ice and ocean circulation using a 3-D, 3.8 km CIOM (Coupled Ice-Ocean Model) under daily atmospheric forcing for the period 1990–2008. The CIOM was validated using both in situ observations and satellite measurements. The CIOM successfully reproduces some observed dynamical processes in the region, including the Bering-inflow-originated coastal current that splits into three branches: Alaska Coastal Water (ACW), Central Channel branch, and Herald Valley branch. In addition, the Beaufort Slope Current (BSC), the Beaufort Gyre, the East Siberian Current (ESC), mesoscale eddies, and seasonal landfast ice are well simulated. The CIOM also reproduces reasonable interannual variability in sea ice, such as landfast ice, and anomalous open water (less sea ice) during the positive Dipole Anomaly (DA) years, vice versa during the negative DA years. Sensitivity experiments were conducted with regard to the impacts of the Bering Strait inflow (heat transport), onshore wind stress, and sea ice advection on sea ice change, in particular on the landfast ice. It is found that coastal landfast ice is controlled by the following processes: wind forcing, Bering Strait inflow, and sea ice dynamics.

1. Introduction

The Beaufort and Chukchi seas (Figure 1) are located in an important region where North Pacific water via the Bering Strait encounters the Western Arctic water and seasonal ice in the Chukchi Sea, and both seasonal and perennial ice in the Beaufort Sea. The Chukchi Sea's main feature is a relatively wide continental shelf, while the Beaufort Sea is characterized by a relatively narrow continental shelf and a deep basin with a narrow, steep shelf slope. More importantly, the Beaufort Sea also features continuous landfast ice along the Alaskan Arctic coast, overlying the 20 m isobath [*Eicken et al*. 2005]. In comparison, the landfast ice along the western Alaska coast in the Chukchi Sea is discontinuous. The ocean circulation system in the Beaufort and Chukchi seas is very complex and consists of the Bering Strait inflow that separates into three branches: the Alaskan Coastal Water/Current (ACW/C), the Central Channel branch, and the Herald Valley branch (see Figure 1). The area also contains the anticyclonic Beaufort Gyre, the Beaufort Slope Current (BSC) [*Pickart*, 2004], and the East Siberian Current (ESC). The BSC has a cross-slope spatial scale of about several dozen kilometers [*Weingartner et al*., 1998; *Pickart*, 2004], and the Barrow Canyon Current has a similar spatial scale of about 30 km to the BSC. Another important feature in the Beaufort Sea is the small mesoscale eddies of a few tens of kilometers in diameter [*Manley and Hunkins*, 1985; *Muench et al*., 2002; *Chao and Shaw*, 2002; *Mathis et al*., 2007; *Watanabe*, 2011], with anticyclones outnumbering the cyclones due to the negative sloping effect relative to the density front orientation [*Ikeda*, 1983; *Wang and Ikeda*, 1997; *Griffiths et al*., 2000], similar to the mesoscale eddies along the Bering Slope Current [*Mizobata et al*., 2006, 2008]. These small mesoscale features can be resolved only with high resolution observation arrays and models.

The winter atmospheric wind pattern is mainly controlled by the anticyclonic (clockwise) Beaufort High, while the summer wind stress is relatively weak due to the weakened Beaufort High. The northward propagating summer storms sometimes move to the Chukchi Sea via the Bering Strait [*Pickart et al*., 2009], producing strong wind and mixing. The winter anticyclonic wind stress associated with the Beaufort High has

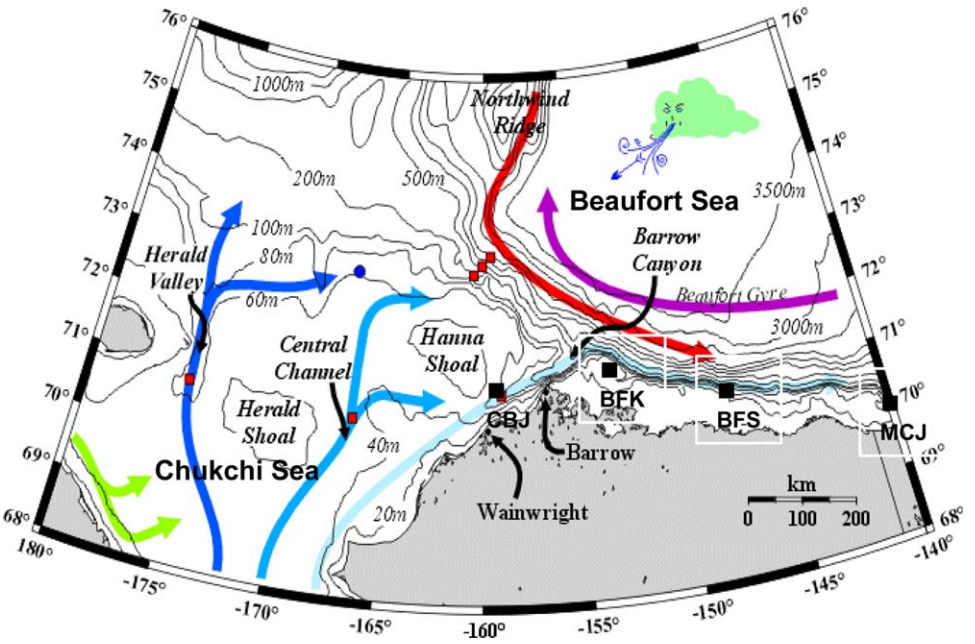

Figure 1. A schematic diagram for coastal circulation in the Chukchi-Beaufort Seas (light blue: Alaskan Coast Current with the origin of freshwater; median blue: Central Branch Current; dark blue: Herald Canyon Branch; red: Bering Slope Current; purple: Beaufort Gyre; green: East Siberian Current.) Depths are in meters (Courtesy of Tom Weingartner). Closed square denotes the mooring stations.

many important effects on (1) surface Ekman drift that advects the Beaufort coastal freshwater into the Beaufort Gyre [*Yang*, 2006], (2) subsurface upwelling that brings the warm, saline Arctic intermediate water (i.e., the Atlantic Water) into the Beaufort Sea shelf break, melting surface sea ice [*Melling*, 1993; *Pickart et al*., 2009], and (3) formation of landfast ice [*Mahoney et al*., 2007a, 2007b].

An extensive review of ocean modeling in the Bering, Chukchi, and Beaufort Seas was given by *Wang et al*. [2009a]. Ocean only models have long been used to investigate ocean circulation in the absence of sea ice [*Nihoul et al*., 1993]. For example, an idealized ocean-only modeling study was conducted by *Winsor and Chapman* [2004] to determine how wind stress, topography, and physical processes affect the Chukchi Sea current system in ice-free conditions. However, without a sea-ice model, ocean-only models cannot reproduce the seasonal cycle of ocean circulation and thermohaline structure.

There has been significant progress in understanding of large-scale Arctic sea ice and ocean circulation through the Arctic Ocean Model Intercomparison Project (AOMIP) [*Proshutinsky et al*., 2001; *Holloway et al*., 2007; *Wang et al*., 2008, and many others]. *Kowalik and Proshutinsky* [1994] developed a 2-D ocean tidal model in the Arctic Ocean. *Chen et al*. [2009] applied a high resolution finite volume ocean model to simulate Arctic tides. In general, most sea-ice models on basin scales use relatively simple thermodynamics and ice thickness distributions. These models can approximate sea ice as slabs of one to a few mean thicknesses as well as open water [*Hibler*, 1979]. While sufficient for simulating Arctic Ocean pack ice for climate study purposes, most present models lack the ability to sufficiently resolve the spectrum of ice thickness from thin, new ice to thick, ridged ice, or to resolve landfast ice anchored along the coast. *Wang et al*. [2002, 2005] developed a pan-Arctic Coupled Ice-Ocean Model (CIOM) with a resolution of 27.5 km, which, of course, is not sufficient to resolve coastal processes and dynamics.

In recent years, eddy-resolving models have been developed and are used to simulate ice and ocean dynamics in the Arctic seas [*Clement et al*., 2005; *Wang et al*., 2008; *Okkonen et al*., 2009; *Zhang et al*., 2010; *Watanabe*, 2011]. Some important processes, including small mesoscale eddies, basin-shelf interaction, and coastal currents, were studied in the Chukchi Sea. Nevertheless, there have been no 2-D modeling studies of landfast ice in the coastal Chukchi and Beaufort Seas, although some field measurements studies were conducted [*Eicken et al*., 2005; *Mahoney et al*., 2007a, 2007b; *Yu et al*., 2013], and 1-D thermodynamic only model was applied to the high Arctic [*Flato and Brown*, 1996].

Landfast ice along the coastline of the Chukchi and Beaufort Seas plays an important role as a biologically productive habitat (such as walrus and polar bears) and transportation corridor. It also provides important protection to the shoreline and coastal installations [*Eicken et al*., 2005]. However, at the present time, it is not clear how the diminishing Arctic summer sea ice [*Wang et al*., 2009a] and the reduction in multiyear ice extent [*Maslanik et al*., 2011] have impacted the seasonal cycle and distribution of landfast ice. Thus, while the seasonal and interannual variability of the landfast ice in a diminishing sea ice scenario in the Chukchi and Beaufort Seas is an important emerging topic [*Wang et al*., 2014], evidence of such variability is somewhat limited. This is largely due to the temporally limited availability of synthetic aperture radar imagery required for accurate assessments of landfast ice extent [*Mahoney et al*., 2007a].

Yu et al. [2013] investigated interannual variability of Arctic landfast ice using observed ice data from 1976 to 2007, including the Beaufort Sea. They found that a significant decrease in landfast ice occurred since 1990. A landfast ice trend in the Beaufort Sea was estimated to be $-0.039\ 10^4\ km^2/yr$.

Model simulations with coupled ice-ocean models can hence provide insight into longer-term variations on time scales of decades, although the modeling of landfast ice at these scales is in its infancy [e.g., *König-Beatty and Holland*, 2010]. *König-Beatty and Holland* [2010] developed a landfast sea-ice model by adding tensile strength to the viscous-plastic as well as two versions of the elastic-viscous-plastic sea ice rheologies. One-dimensional implementations of these rheologies are used to explore the ability of coastal sea ice to resist offshore winds over extended times. While all modified rheologies are capable of maintaining landfast ice-like structures in the model, only the viscous-plastic rheology fulfills theoretical expectations. Again, these 1-D models also do not have any anchoring mechanism and sea ice dynamics. Because a one-dimensional thermodynamic only model was used to simulate Arctic landfast ice thickness at only a point [*Flato and Brown*, 1996], it lacks some important dynamic processes, such as sea ice dynamics like internal ice advection, ocean current and wind advection, geometric configuration, and bottom anchoring among others.

Landfast ice along the Chukchi and Beaufort coast is a seasonal phenomenon with interannual variability [*Eicken et al*., 2005; *Mahoney et al*., 2007a]. It is a great challenge for any coupled ice-ocean model to capture the dynamic and thermodynamic features of landfast ice, since many factors can affect the formation, anchoring, and melting of landfast ice, such as wind forcing, ocean currents, and coastal topography and bathymetry.

Although the present ice models have no anchoring mechanism for coastal landfast ice, we attempt to investigate and explain the observed measurements using the existing CIOM with multicategory thickness (i.e., with ridging mechanism) and possibly advocate for future research in anchoring formulation of landfast ice dynamics and thermodynamics. The goal of this study is to investigate some important mesoscale dynamic and thermodynamic features of both the ocean circulation and sea ice processes (such as mesoscale eddies, landfast ice, BSC, Bering Strait inflow, and ice advection) in the Chukchi and Beaufort Seas using an eddy-resolving (3.8 km), state-of-the-art, stand-alone coupled ice-ocean model. We will focus on seasonal and interannual variability of coastal ocean circulation and landfast ice in the nearshore Chukchi and Beaufort Seas.

2. Model Description, Configuration, Forcing, and Observations

2.1. Description of CIOM

Detailed description of the CIOM can be found in *Yao et al*. [2000] and *Wang et al*. [2002, 2005, 2009a]. The ocean model used is the Princeton Ocean Model (POM) [*Mellor*, 2004], and the ice model used is a full thermodynamic and dynamics model [*Hibler*, 1979, 1980] that prognostically simulates sea-ice thickness, sea ice concentration (SIC), ice edge, ice velocity, and heat and salt flux through sea ice into the ocean. The model has been successfully applied to the Bering Sea [*Hu and Wang*, 2010; *Hu et al*., 2011; *Wang et al*., 2009b], the Beaufort Sea [*Wang et al*., 2003, 2008], the Arctic Ocean [*Wang et al*., 2005; *Long et al*., 2012], and in the Great Lakes [*Wang et al*., 2010b].

2.1.1. Ocean Model

1. Horizontal spherical grid with 3.8 km resolution in longitude and latitude covering the Chukchi-Beaufort seas;

Table 1. JAMSTEC Mooring Stations, Observation Duration, Bottom Depth, ADCP Instrument Depth, Vertical Resolution, and Record Time Interval

Station	Observed Duration	Bottom Depth/m	Instrument Depth/m	Vertical Resolution/m	Time Interval/h
CBJ	9/92-7/97	75	10–56	2	0.5
BFK	7/98-10/99	132	82–126	4	1
BFS	7/98-10/99	513	101–250	101, 192, 413	1
MCJ	10/99-10/00	260	164–243	164, 243	1

2. Twenty-four sigma levels in the vertical;

3. Open boundaries (velocity, T, and S) are embedded by a climate (atmosphere-ice-ocean-land) GCM from Japan with a resolution of about 25 km [*Watanabe et al*., 2006] with volume transport conservation principles and radiation properties [*Wang et al*., 2001];

4. Inclusion of parameterization of wind-wave mechanic mixing [*Hu and Wang*, 2010];

5. Atmospheric forcing uses National Centers for Environmental Prediction (NCEP) Reanalysis products: heat flux, mass (moisture) flux, and 6 hourly wind stress.

2.1.2. Ice Model

1. Full thermodynamics;

2. Full dynamics with plastic-viscous rheology [*Hibler*, 1979; *Wang et al*., 1994] under the NCEP forcing;

3. Multicategory ice model [*Thorndike et al*., 1975; *Hibler*, 1980; *Yao et al*., 2000] fully coupled to an ocean model [*Mellor and Kantha*, 1989; *Kantha and Clayson*, 1994];

4. Inclusion of lateral melting of sea ice [*Ohshima and Nihashi*, 2005];

5. Prognostic and diagnostic variables: Ice velocity, compactness, ice edge, thickness, heat budget, salt budget, ice stress, etc.

In this study, 10 ice categories (0, 0.2, 0.5, 1, 1.5, 2, 3, 4, 5, and 6 m) are used, each having a percentage in a grid point. Thus, a thickness equation for each category is calculated. Then, the summation of each category thickness is the total thickness at each grid. Thus, sea ice concentration and thickness at each grid are calculated from the sum of the 10 ice categories.

The model was spun up with the PHC temperature and salinity [*Steele et al*., 2001], sea ice climatology, January concentration, and motionless sea ice and ocean for the first 4 years under NCEP reanalysis monthly climatological atmospheric forcing, which were derived (averaged) from 1958 to 2008. At the bottom layer, both temperature and salinity are restored to the monthly climatology with the same time scale of 60 days. At the surface, salinity, with freshwater flux forcing from *P-E*, is restored to the observed monthly salinity fields at a time scale of 30 days for prescribing freshwater runoff into the Arctic Basin using the flux correction method of *Wang et al*. [2001]. After a 4 year spin-up, a dynamic and thermodynamic seasonal cycle is established. Then, we reran the model using the daily NCEP forcing to drive the CIOM from 1990 to 2008 for year-to-year variability.

2.2. Measurements

JAMSTEC (Japan Agency for Marine-earth Science and TEChnology) conducted its biannual field campaigns aboard the *R/V Mirai* in the Beaufort and Chukchi seas. Data collection includes ship-board CTD (conductivity-temperature-depth), towed ADCP (acoustic Doppler current profiler), moored ADCP, CTD, current meters, and biogeochemical sensors (http://www.jamstec.go.jp/arctic). The data used here are from 1992 to 2000. A summary of these data is given in Table 1. These data are used as independent observations to validate the CIOM.

Satellite remotely sensed data sets were employed to validate the CIOM. To compare the sea ice area, we used the sea ice concentration maps derived from the Special Sensor Microwave Imager (SSM/I) on board the Defense Meteorological Satellite Program (DMSP) F-13. This product is available at the National Snow and Ice Data Center (NSIDC) website (http://nsidc.org/data/sea_ice.html#SEA_ICE_CONCENTRATION). There are two algorithms for sea ice concentration: the NASA team algorithm [*Cavalieri et al*., 1990] and the

Bootstrap algorithm [*Comiso*, 1990]. The NASA team algorithm takes into account the multiyear ice fraction, while the Bootstrap algorithm assumes open water and ice.

In this study, the NASA team algorithm was selected to evaluate sea ice concentration from 1998 to 2008. The horizontal resolution is 25 km, and the map projection is the polar stereographic. Extraction of data and converting from the Polar stereographic projection to the cylindrical projection (9 km) were done using Interactive Data Language (IDL).

To compare the CIOM temperature field with the satellite data set, we used the AVHRR Oceans Pathfinder Global 4 km Equal-Angle All SST V5 provided by the NASA/Jet Propulsion Laboratory/Physical Oceanography Distributed Active Archive Center (PO. DAAC; http://podaac.jpl.nasa.gov). The accuracy of this pathfinder SST is 0.3°C. Horizontal resolution is 4 km. We also utilized the Moderate Resolution Imaging Spectroradiometer (MODIS) Level 3 mapped standard product suite SST. Data processing was conducted by the SeaWiFS Data Analysis System (SeaDAS 5.0; ttp://oceancolor.gsfc.nasa.gov/seadas/) [*Fu et al*., 1998].

3. Results

3.1. Validation of Ocean Circulation Pattern Using In Situ Observations

The high resolution CIOM reproduced very fine structure of the Alaskan Coastal Current system (three branches) and the anticyclonic large-scale Beaufort Gyre superimposed by mesoscale eddies with anticyclones outnumbering cyclones (Figure 2). The first branch is the Alaskan Coastal Water (ACW) branch along the Alaska Arctic coast. This current flows mainly along the isobaths with relatively warm water, hugging to the Alaska coast. The second branch (middle) flows northward along the Central Channel and turns to the east, joining the ACW. The ACW flows eastward all the way to the Canadian Beaufort Sea, encountering the Mackenzie River outflow, where the coastal current then turns sharply to the west and joins the Beaufort Gyre (westward) circulation. As a consequence, between the Beaufort Gyre and ACW current there is a strong horizontal shear, resulting in a deep trough in sea surface height (SSH). This phenomenon is found for the first time using this high resolution CIOM and needs field measurements to confirm its existence. The third branch flows northwestward into the Chukchi Sea via a deep channel between Wrangel Island and Herald Shoal. Part of this current turns to the east and joins the Beaufort Slope Current (BSC) [*Pickart*, 2004]. In addition, the ESC is also reproduced. These features are consistent with recent observations in the region [*Woodgate et al*., 2005]. The simulated Beaufort Gyre is confirmed by the high SSH (red) with anticyclones dominating due to baroclinic instability [*Wang and Ikeda*, 1997; *Chao and Shaw*, 2002].

The simulated annual average current velocity at 70 m compares reasonably well with the moored ADCP-measured velocity (Figure 3a) at four locations. Figure 3a shows the comparison between the model simulated velocity (black) and the ADCP mooring velocity (red) at a subsurface layer of 70 m. The simulated velocities are, in general, consistent with the observed. There are discrepancies in both direction and magnitude, which may be because (1) the model topography/depth was smoothed and (2) the model vertical and horizontal resolution was still coarse. The model basically captures the vertical structure of the mean flow (Figure 3b) in the Beaufort Sea (the second station from left) with the alongshore component (u) being better reproduced than the offshore component (v).

3.2. Validation of Sea Ice Using Satellite Measurements

To evaluate the CIOM, we compared the simulated results with satellite measurements. Figure 4 shows the time series of the averaged sea ice area derived from SSM/I measurements between 1997 and 2005 (black line), the sea ice area in 2002 (blue line), and the sea ice area in 2002 simulated by the CIOM (red line). In Figure 4, we plotted a 3 day averaged sea ice area estimated from the CIOM output, so that short-term variability, which is shown by the SSM/I measurements, is reduced. However, the CIOM accurately reproduces the seasonal cycle of sea ice in the Chukchi/Beaufort Sea, while the simulated sea ice was suddenly melted in late July due to the imposed lateral melting parameterization. The maximum sea ice area and the timing of ice melting/freezing are consistent with SSM/I measurements. Also, sea ice freezing during winter (October–December 2002) was accurately reproduced. During August 2002, the open water area was larger in the simulation than what was measured by the SSM/I. The melting rate of sea ice from May to August and the maximum sea ice retreat still need to be improved. The ice melting rate is slow during May and early June and fast during late July and August when compared with the SSM/I measurements.

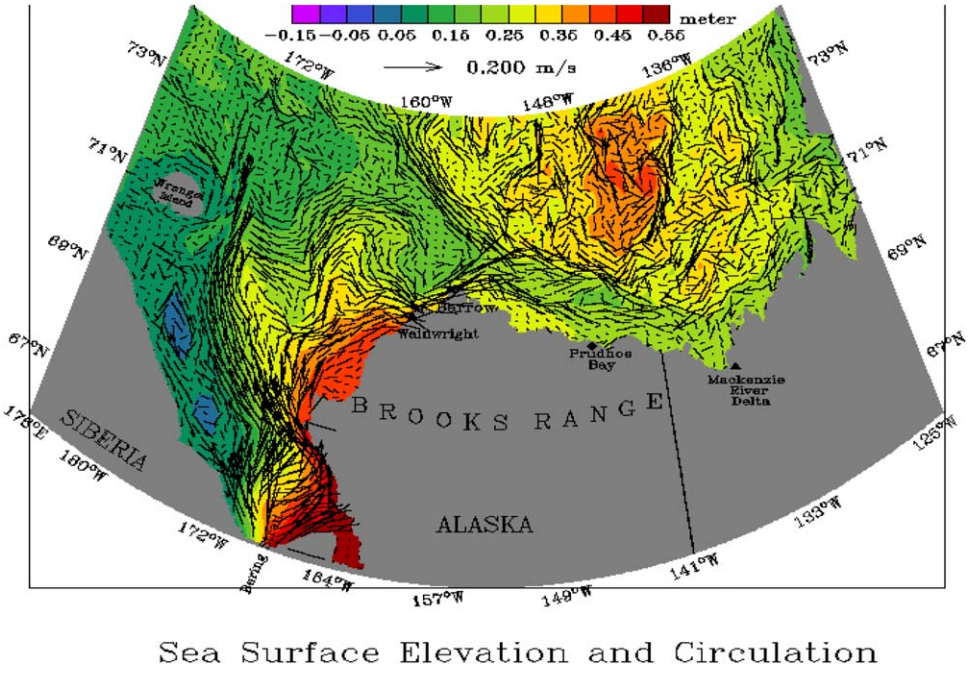

Figure 2. Model-simulated upmost 50 m averaged ocean velocity and sea surface height (elevation in color with units of meters) on 10 July 2002, consistent with the schematic ocean circulation pattern (Figure 1).

3.3. Ocean Circulation and Mesoscale Eddies in the Chukchi and Beaufort Seas

In the Chukchi Sea shelf, warm Pacific water intrudes through the Bering Strait. Heat input through the Bering Strait can cause rapid sea ice reduction [*Shimada et al*., 2006; *Wang et al*., 2009a; *Woodgate et al*., 2010; *Mizobata et al*., 2010]. Figure 5 shows AVHRR daily sea surface temperature images on 21 July (Figure 5a), 1 August (Figure 5c), and 22 September (Figure 5e) of 2002 and ice-ocean circulation (Figures 5b, 5d, and 5f) simulated by the CIOM in the Chukchi Sea. SST patterns are similar to the ocean temperature simulated by the CIOM. Both AVHRR SST and ocean temperature derived from the CIOM show warm water covering the Chukchi Sea in July (Figures 5a and 5b), extending to the Herald Canyon, the western Hanna Shoal, and the southeastern Siberian coast in August (Figures 5c and 5d). The warm water pattern greater than 8°C was captured by the AVHRR and indicates the ACW branches (Figure 5c). Those features were well simulated by the CIOM, except for magnitude of temperature (Figure 5d). The AVHRR SST indicates the warm Alaskan Coastal Current flowing along the Alaska coast. Warm water reached the Icy Cape in August (Figure 5c) and the Barrow Canyon in September (Figure 5e). The CIOM results are consistent with satellite measurements and previous ship surveys. Thus, the distribution of the warm Pacific water and ocean circulation in the Chukchi Sea were well simulated. A big difference between AVHRR images and CIOM results is the high water temperature core at the Siberian coast (Figures 5a and 5c). Currently, this high water temperature core is not well simulated. A similar warm core was found in July 2004 in satellite measurements (not shown). No documents exist showing this feature. If this warm core is a real phenomenon, it would affect the timing and pattern of sea ice freezing and melting; further investigation is needed. A cold band at the Siberian coast in September is due to errors resulting from cloud or fog.

During the open water period, small-scale eddies with radii as small as 10–20 km have been observed in the Beaufort Sea basin area [*Manley and Hunkins*, 1985; *Muench et al*., 2002; *Spall et al*., 2008]. Figure 6 shows a snapshot of the simulated result on 24 September 2002. Red boxes indicate the eddy field. There are two main streams of warm Pacific water having a north-south component in water velocity, implying a small mesoscale eddy field. Eddies also can be found near the ice-edge.

The mechanism for generation of these small mesoscale eddies was theoretically investigated by *Ikeda* [1983] and further using 3-D numerical models with sloping bottoms by *Wang and Ikeda* [1997] and *Griffiths et al*. [2000]. *Wang and Ikeda* [1997] found that the sloping bottom, both positive and negative sloping

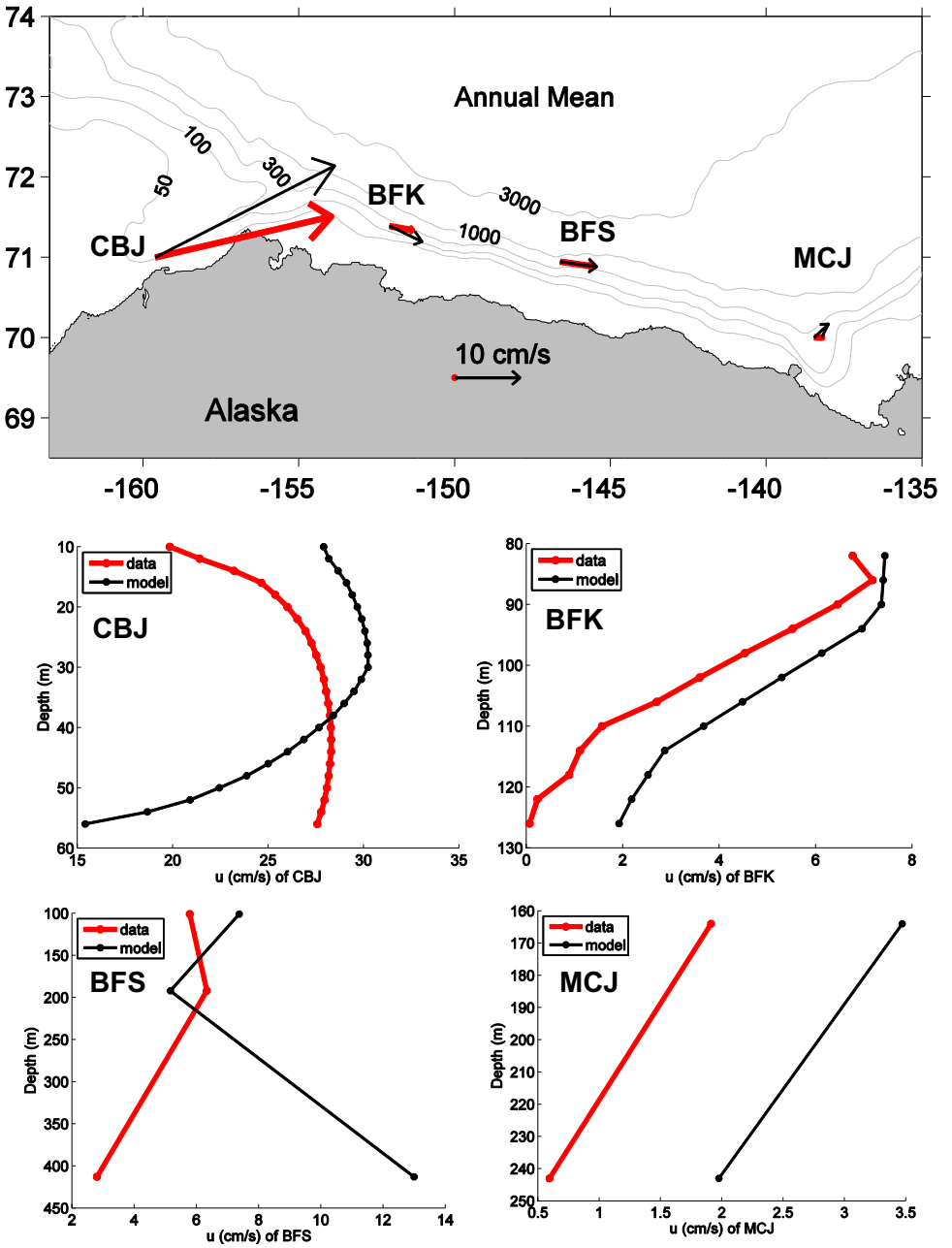

Figure 3. (top) Annual mean and depth-average velocity reproduced by the model (black) is compared to the JAMSTEC ADCP-measured velocity (red) and annual-average vertical profiles of observed alongshore velocity (red) and modeled velocity (black) at all four moorings, as indicated, in the Beaufort and Chukchi seas.

topography have a significant impact on the sizes of mesoscale eddies and their growth rate. The positive (negative) sloping topography is defined as the same (opposite) inclination between the frontal density distribution and sloping orientation. For example, the Kuroshio and the Gulf Stream have a positive sloping bottom, while the Labrador Current, the Bering Slope Current, and Beaufort Slope Current have a negative sloping bottom. Therefore, along the negative slope in the nearshore Chukchi and Beaufort Seas, the eddies growth rate is dampened and shifted to higher wave numbers. In other words, the negative slope promotes short mesoscale eddies (waves), while dampening the long waves [*Wang and Ikeda*, 1997, see Figure 6]. This is similar to the Bering (negative) Slope (Current): (1) there are always small mesoscale eddies and (2) there are more anticyclone eddies than cyclone eddies, as observed and simulated by *Mizobata et al.* [2006, 2008].

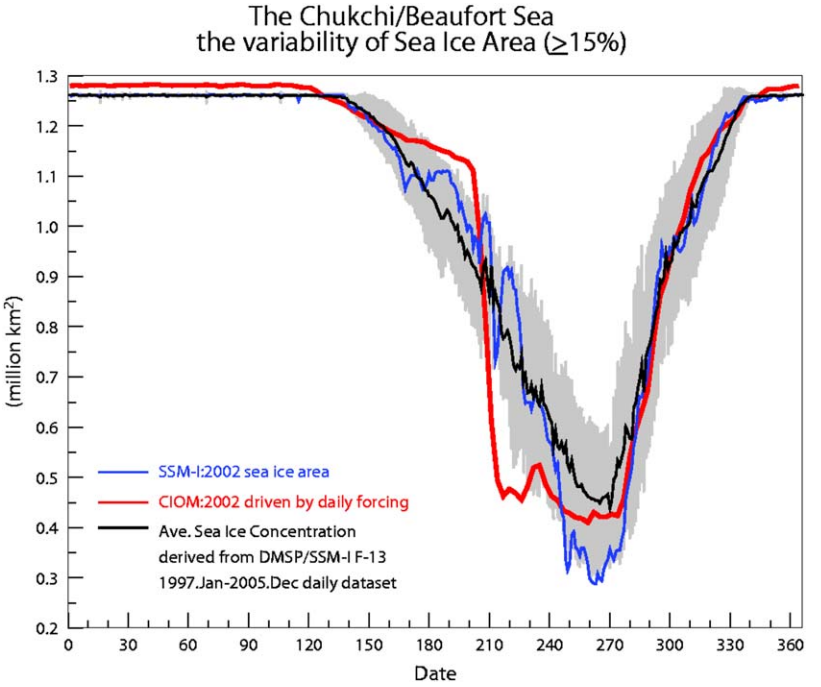

Figure 4. Seasonal cycle of sea ice area in the Chukchi/Beaufort Sea derived from the SSM/I measurements (blue line, daily) and simulated by the CIOM (red line, 3 day averaged). Sea ice concentration less than 15% was ignored to avoid the error of SSM/I measurement. Gray area shows the variance of the averaged sea ice area from 1997 to 2005. Black line shows the average sea ice area derived from DMSP/SSMI F-13 from 1997 to 2005.

Hart and Killworth [1976] pointed out that such small mesoscale eddies with observed radii of 10–20 km cannot be generated in the deep Arctic basin, but possibly between 50 and 300 m of the (negative) sloping bottom. *Chao and Shaw* [2002] also used an idealized channel model to investigate these small eddies due to baroclinic instability.

To further understand the mechanism for generating such small mesoscale eddies, we applied a theoretical, three-layer model developed by *Ikeda* [1983] to explain why the modeled small mesoscale eddies are consistent with the theoretical estimate. The Alaska Coastal Current has the following parameters: upper layer with thickness is $H = 100$ m; density difference from the layer below is $\Delta\rho = 2$ kg m^{-3}; and Coriolis parameter is $f = 1.4 \times 10^{-4}$ s^{-1}. Thus, the internal Rossby radius is $L = (g\Delta\rho H/\rho_o)^{-1/2}/f = 10^4$ m $= 10$ km. This Rossby radius is associated with the upper layer much thinner than the lower layer, where g is the gravitational acceleration and ρ_o is water density. The typical current speed is $U = 0.1$ m s^{-1}; Rossby number is calculated as $Ro = U/(fL) = 0.07$; bottom slope (typical value taken as an example with a depth increase of 1000 m over distance of 100 km) is $H_y = 1/100$ where H_y is scaled by $(R_o\ H_o)/L = 0.07 \times 1000/10^4 = 0.007$. Thus, nondimensional bottom slope is 1.4.

In *Ikeda* [1983, Figure 4], if we assume a two-layer system (with very small density variability in the lower layer), the wave number is about 1.5 times of the flat bottom case. The wavelength becomes 0.7 times of the flat bottom case. In *Ikeda* [1983, Figure 3], if we assume a three-layer system (with some density difference in the lower layer), and the third layer has no motion, then, the system acts as a two-and-half layer model. Therefore, the bottom slope has minor effect on the wavelength, except for a narrow branch at larger wave number.

The wavelength is calculated to be (2π/wave number) L. In *Ikeda* [1983, Figure 7], the flat bottom case gives the wave number (0.7) of the fastest growing mode. Thus, ($2\pi/0.7$) $\times$ 10 km $=$ 90 km. Over the continental slope, the wave number could be as large as 1.2. Then, the wavelength is 50 km. There are no straightforward ways to estimate the diameter of a detached eddy. If we simply take 1/3 of the wavelength, then the diameter of an eddy is about 30 km without the bottom topography effects, while it is slightly smaller less than 20 km with the negative sloping bottom [*Wang*

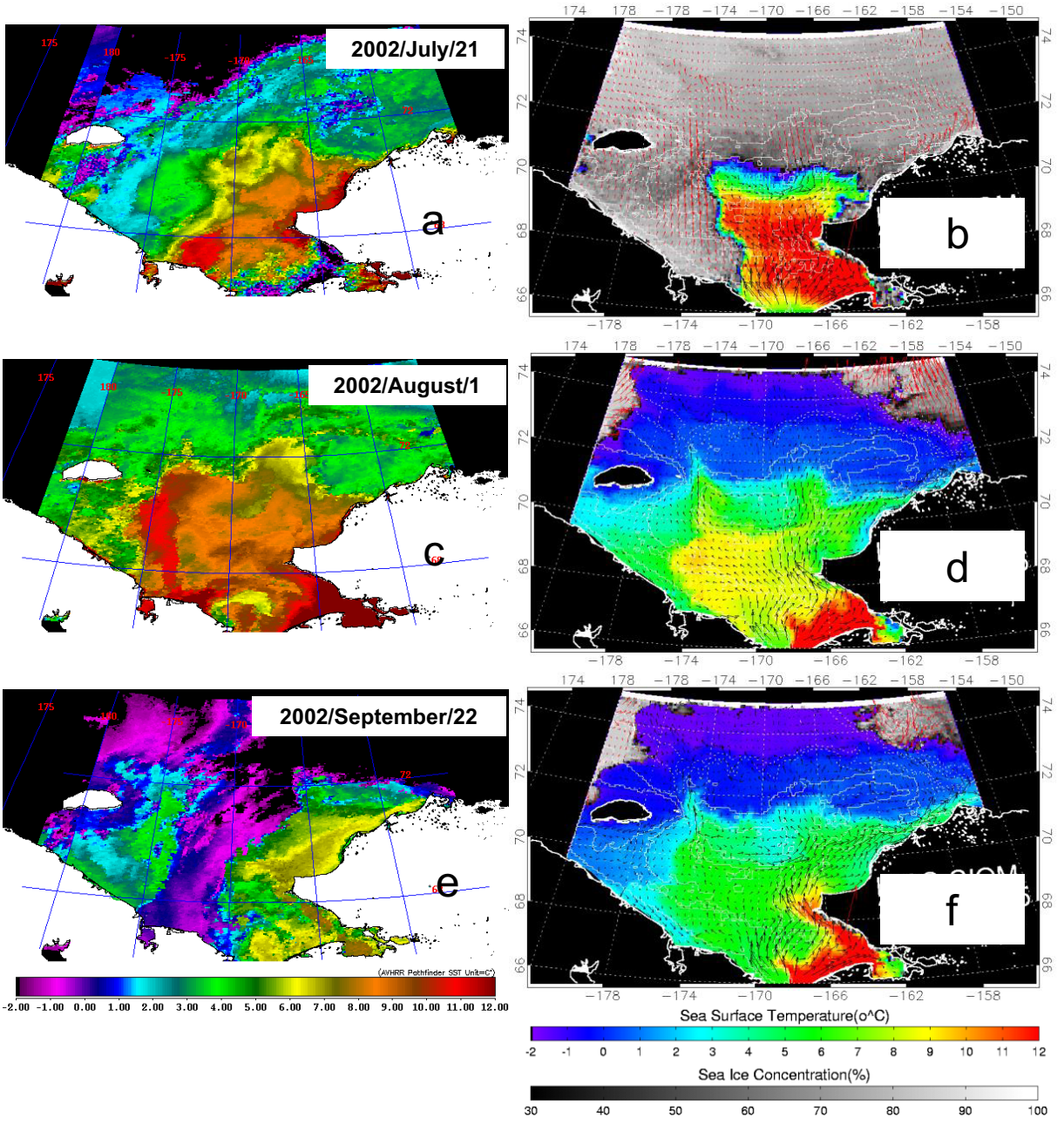

Figure 5. AVHRR-derived daily sea surface temperature images on (a) 21 July, (c) 1 August, and (e) 22 September (left) of 2002 and simulated ice-ocean circulations (b, d, and f) in the Chukchi Sea.

and Ikeda, 1997]. This estimate is also consistent with the theoretical analysis of *Hart and Killworth* [1976].

3.4. Landfast Ice in the Nearshore Beaufort Sea

The ice-ocean circulation system experiences a seasonally repeated cycle in the nearshore Beaufort Sea. Sea ice distribution is influenced not only by thermodynamics but also by the ACW coastal current, small mesoscale eddies, river discharge, and the Beaufort gyre. Figure 7 shows the CIOM results from August to November. Water velocity is plotted at every grid point (black arrows) because the scale of eddies is small (10–20 km) due to the fact that the Rossby radius of deformation is about 5 km [*Watanabe*, 2011] and has a

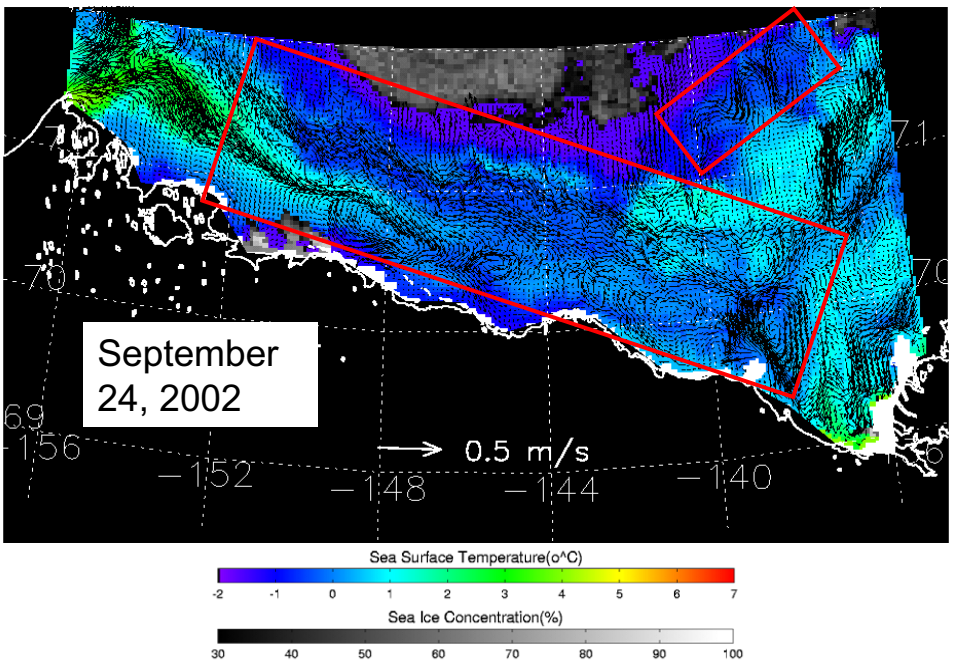

Figure 6. A snapshot of the CIOM simulation in the Beaufort Sea (24 September 2002). Black arrows represent water velocity at 10 m water depth at each grid cell. Inside the red boxes, small mesoscale eddies are active, with anticyclones outnumbering cyclones.

negative sloping topography [*Wang and Ikeda*, 1997; *Griffiths et al*., 2000]. In August, open water was formed and warm Pacific water came from the Barrow Canyon. There was another source of heat from the Mackenzie River. Sea ice in the basin had melted, but the landfast ice still remained at the Alaska coast between 156°W and 144°W (Figures 7a–7c). SSM/I measurements also indicate the landfast ice along the Alaska coast in August (Figure 8). During September, wide open water and meandering of the boundary current resulting from eddies were simulated (Figures 7d–7f). In October, the boundary current was close to the Alaska coast (6 October, Figure 7g), and sea ice began forming. In November, the CIOM simulated sea ice freezing and the polynya in the Beaufort basin (Figures 7h and 7i). According to Figure 7, sea ice cover resulted from ice production at the coast (landfast ice) and in the basin, and ice advection from the basin to the Alaskan coast. Ice was produced at the Alaskan coast due to the shallow water depth, resulting in rapid freezing. On the other hand, SSM/I measurements show that sea ice cover is due to ice production in the basin area or advection from north or east (Figure 8). Wide landfast ice was not seen in October from SSM/I measurements possibly due to the coarse resolution (25 km), compared to the 3.8 km resolution CIOM. Due to coastal sea fog, the SSM/I measurements may also overestimate SIC along the coast by 10–15%, particularly in summer. Therefore, there is a need to validate landfast ice production.

Figure 9 shows the 10 year (1994–2004) seasonal climatology (mean) of minimum, mean, and maximum landfast ice extents in the Beaufort Sea, measured by SAR and SSM/I [*Eicken et al*., 2005]. Landfast ice starts to form in October, and steadily increases in area from November to February, and reaches a maximum in March and April. In May, landfast ice starts to decay and reduces in area. From June to July, the area significantly reduces.

There are several approaches to distinguish landfast ice from pack ice in a model. One way is to define landfast ice by an ice velocity criterion that considers ice stationary below a given velocity threshold. In this study, if *both* the absolute ice velocity is less than 4 cm/s, and the water depths are less than 35 m, then grid cells are designated as landfast ice. In this study, we use this empirical method to identify the landfast ice from pack ice. The second, prescriptive method stipulates that during the simulation, the wind stress, and ice velocity are set to zero shoreward of the 35 m isobaths, roughly corresponding to the extent of landfast ice in many areas. However, this method sometimes causes model instability due to the fact that ice mass balance is not met because the ice velocity is artificially and forcefully set to zero. Therefore, we

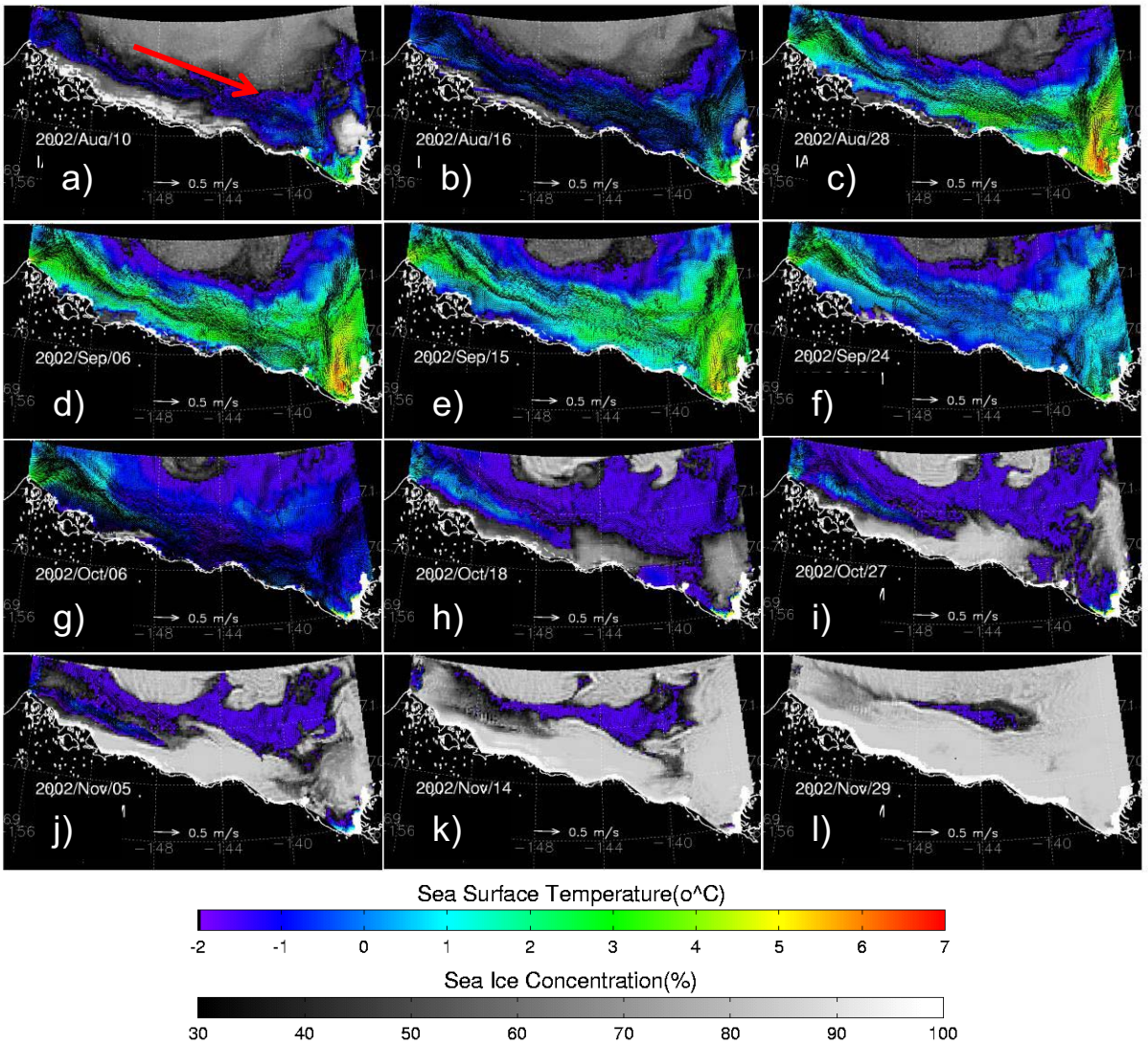

Figure 7. Sea ice cover and ocean circulation in the Beaufort Sea coastal area on (a) 10 August, (b) 16 August, (c) 28 August, (d) 6 September, (e) 15 September, (f) 24 September, (g) 6 October, (h) 18 October, (i) 27 October, (j) 5 November, (k) 14 November, and (l) 29 November in 2002 simulated by the CIOM. Gray area shows sea ice concentration between 30% and 100%. Black arrows indicate water velocity (10 m water depth) at every grid point.

did not use this method in this study. The third method is to mask out the landfast ice grids during model simulation based on existing observation. In other words, over these masked landfast grids, no dynamic equations are used to integrate along with the pack ice dynamics. The second method is widely used in Baltic Sea ice simulations [*Haapala et al*., 2001; *Meier*, 2002a, 2002b], which is not capable of representing spatial and interannual or seasonal landfast ice extent.

Figure 10 shows the climatology (1996–2004) of the simulated landfast ice that was compared to observed landfast ice extents obtained from synthetic aperture radar satellite data for the period 1996–2004 [*Eicken et al*. 2005; *Mahoney et al*., 2007a]. In the model, landfast ice starts to form in autumn due to the Beaufort Gyre and anticyclonic winds induced by the Beaufort High, both of which push sea ice toward the Alaskan Beaufort coast, coupled with the thermal growth of sea ice along the shore [*Wang et al*. 2009a]. When sea ice completely covers the entire Arctic beginning in December, landfast ice is attached to shore, while pack ice offshore still moves with the ocean surface current and wind forcing. During the period of complete ice cover, the radar satellite data indicate completely stationary landfast ice with a clearly delineated boundary between pack ice and landfast ice (anchored to the bottom and attached to shore with the velocity almost

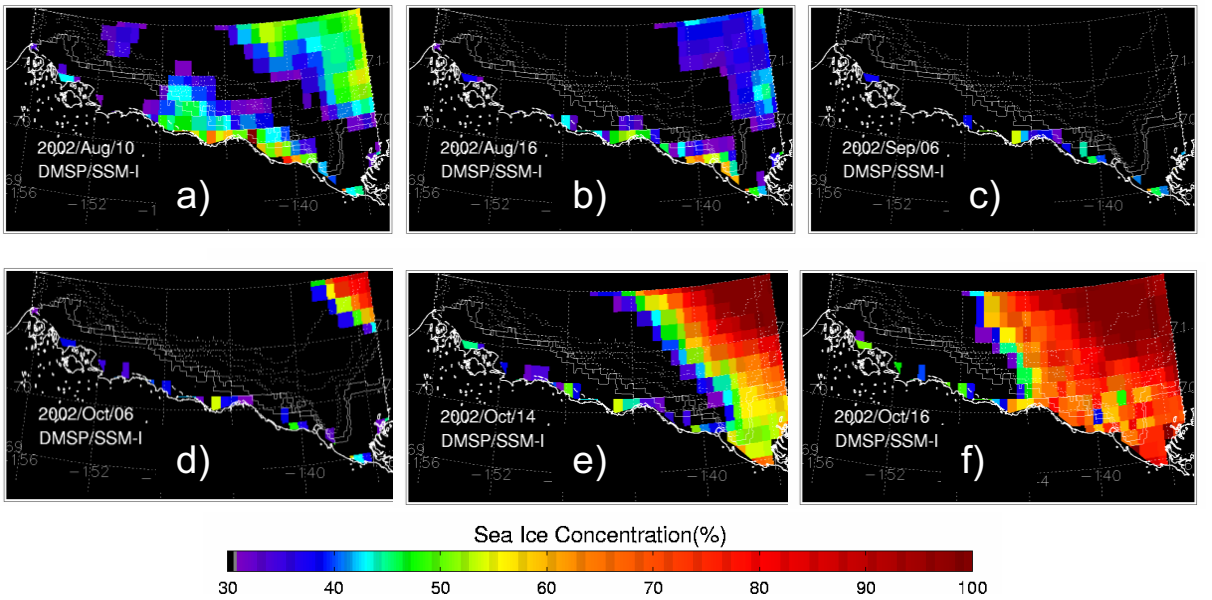

Figure 8. SSM/I sea ice concentration images in the Beaufort basin area on (a) 10 August, (b) 16 August, (c) 6 September, (d) 6 October, (e) 14 October, and (f) 16 October. Note that the resolution is 25 km.

being zero), while the CIOM-simulated landfast ice still exhibits small movement, since the sea ice produced in the CIOM is not resolving the anchoring of grounded pressure ridge keels that stabilize the landfast ice. Thus, more research is required to improve the representation of ice dynamics in coastal regions and landfast ice processes by formulating and including the relevant ice anchoring mechanisms in the model.

The CIOM-simulated landfast ice is generally consistent with landfast ice extent derived from satellite data. The CIOM reproduces the landfast ice boundary in January and February very well. However, the model reproduces less landfast ice than the measured boundary in March. During April, the CIOM reproduces landfast ice reasonably well in general, but reproduces less ice from 147°W to 152°W. In May, CIOM reproduces more landfast ice between 140°W and 147°W. In June, the model simulation compares very well with measurements.

To investigate the interannual variability of the landfast ice, we first calculate the seasonal cycle of the landfast ice area based on those grid cells conforming with the ice velocity criterion described above and exhibiting an ice concentration greater than 0.8 within 160°W–134°W for the period of 1990–2007 (Figure 11a). Three characteristics are apparent: (1) landfast ice exhibits a uniform extent indicative of overall stability of the ice cover from January to April with a maximum in April; (2) the largest variability (i.e., standard deviation) occurs in June and November, during the peak of the melt (decay) and freezeup (formation) seasons, respectively; and (3) there is no landfast ice in September.

Figure 11b shows the year-to-year variability of the landfast ice area. One striking feature is that the landfast ice formed earlier and melted later before 1998, however since then, the duration of the landfast ice season has shortened significantly since 1998, consistent with the results of *Yu et al.* [2013]. This is consistent with the increase in Bering Strait heat transport since 2001 [*Woodgate et al.*, 2010], particularly since 2004 when both temperature and volume transport increased. In the spring of 2007, landfast ice decayed more rapidly than in the previous years (2004–2006), since the +DA-derived wind anomaly was directed offshore (i.e., northward) [*Wang et al.*, 2009a], in addition to other forcings such as maximum Bering Strait heat transport [*Woodgate et al.*, 2010; *Mizobata et al.*, 2010], and ice/ocean and cloud albedo feedbacks [*Ikeda et al.*, 2003; *Wang et al.*, 2005], leading to thinner pack ice. Figure 11c shows the time series of landfast ice area anomalies for 1990–2007. It is clear that from 1990 to 1997, positive anomalies dominated, but since then, Beaufort and Chukchi Sea landfast ice extent was characterized by negative anomalies. As evident from Figure 11b, these anomalies are not due to reductions in maximum extent, but rather driven by shifts in the seasonality

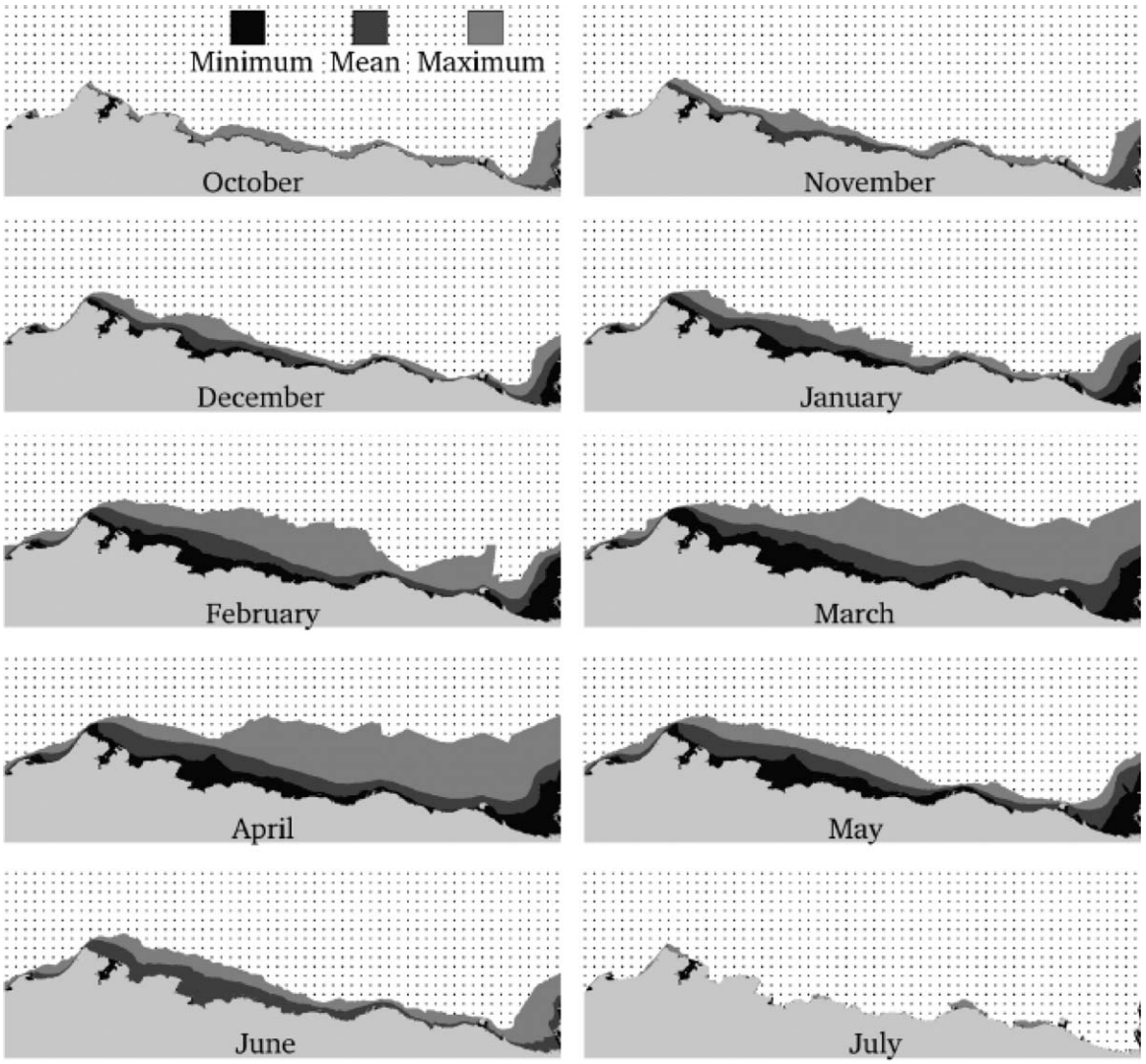

Figure 9. Minimum, mean, and maximum monthly landfast sea ice extents showing the change in landfast ice distribution in the study area through the annual cycle. The dotted area indicates where landfast ice was never observed [from *Eicken et al*., 2005].

of the landfast ice, i.e., the shortened duration. This finding is in line with observations by *Mahoney et al*. [2007a] and points to the importance of decadal-scale variations in landfast ice extent.

A 5 year running mean (dashed line of Figure 11c) indicate possible decadal variability in landfast ice, driven by atmospheric forcing and oceanic forcing such as global teleconnection patterns and Bering Strait oceanic heat transport. Similar to *Yu et al*. [2013], a trend in landfast ice area was calculated (solid line of Figure 11c). The negative trend has a rate of -0.048×10^4 km^2/yr between 1990 and 2007, which is consistent with, but slightly larger than the rate of -0.039×10^4 km^2/yr between 1976 and 2007, derived by *Yu et al*. [2013, see their Table 1]. The larger rate is due to the different length of the two time series. Since 1990, +DA events were intensified and occurred more frequently than the period 1976–1990. This trend is consistent with reduction in Arctic summer sea ice [*Wang et al*., 2009a] and multiyear ice [*Maslanik et al*., 2011] due to intensified positive Arctic Dipole Anomaly (+DA) activity [*Wang et al*., 2009a], and with increase in northward oceanic heat transport through Bering Strait [*Woodgate et al*., 2010].

To further explain the impacts of DA on landfast ice, similar to the pack ice [*Wang et al*., 2009a], we conduct a composite analysis in the following.

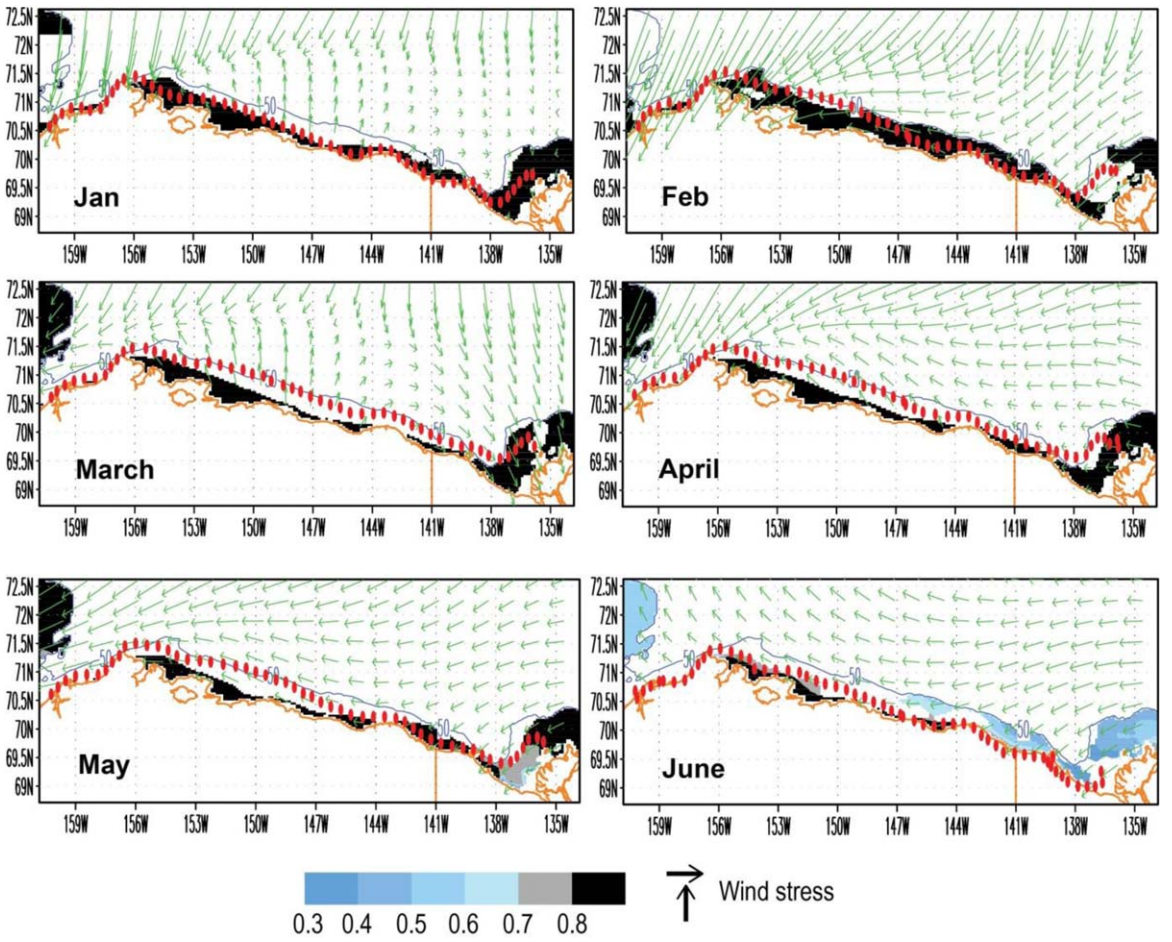

Figure 10. The CIOM-simulated January to June climatological landfast ice extent (from 1996–2004, black shaded) compared to landfast ice edge locations derived from synthetic aperture radar satellite data (red dots) averaged for the period 1996–2004. Green vectors are wind stress in units of 10^{-5} N m^{-2}.

4. Interannual Variability of Sea Ice in Response to DA

During the study period, the Arctic Oscillation (AO) was weakened [*Wang and Ikeda*, 2000, 2001], and the Arctic Dipole Anomaly (DA) [*Wu et al*., 2006; *Watanabe et al*., 2006; *Wang et al*., 2009a] was intensified. The positive (negative) DA-derived anomalous meridional wind stress along (against) the Trans-polar Drift Stream (TDS) toward the eastern (western) Arctic produced anomalous more (less) open water in the Alaskan Beaufort Sea, and thus anomalously less (more) landfast ice along the coast.

We have conducted multiple year simulations from 1990 to 2008 to investigate the interannual variability. Large interannual variations in summer ice concentration (or open water) in the Alaskan Beaufort Sea are caused not only by atmosphere but also by ice-ocean nonlinear feedbacks [*Wang and Ikeda*, 2001; *Maslanik et al*., 2007]. Two phases of DA years were chosen: +DA (1995, 1999, 2005, 2007), and –DA (1996, 1998, 2003, 2004) to conduct a composite analysis. The average +DA index of these years is +1.56, and the average –DA is −0.88, indicating that the +DA events were stronger than the –DA during the study period. Figure 12 shows spatial composite average in July (melting season) and in November (freezing season) for the +DA and –DA years. In July, there was less sea ice cover (smaller concentration) during the +DA phase (Figure 12a) than the –DA phase (Figure 12b) because the stronger warm Bering Strait inflow reached further north during the +DA phase than the –DA phase. Obviously, there was more landfast ice cover during the –DA phase than the +DA phase along the Beaufort coast. The concentration difference (C_diff = −DA minus +DA) field (Figure 12e) indicates that there was a positive anomaly of 0.1 along the Beaufort coast and of 0.2–0.3 in the central Beaufort Sea. The thickness difference field (Figure 12f) also shows overall

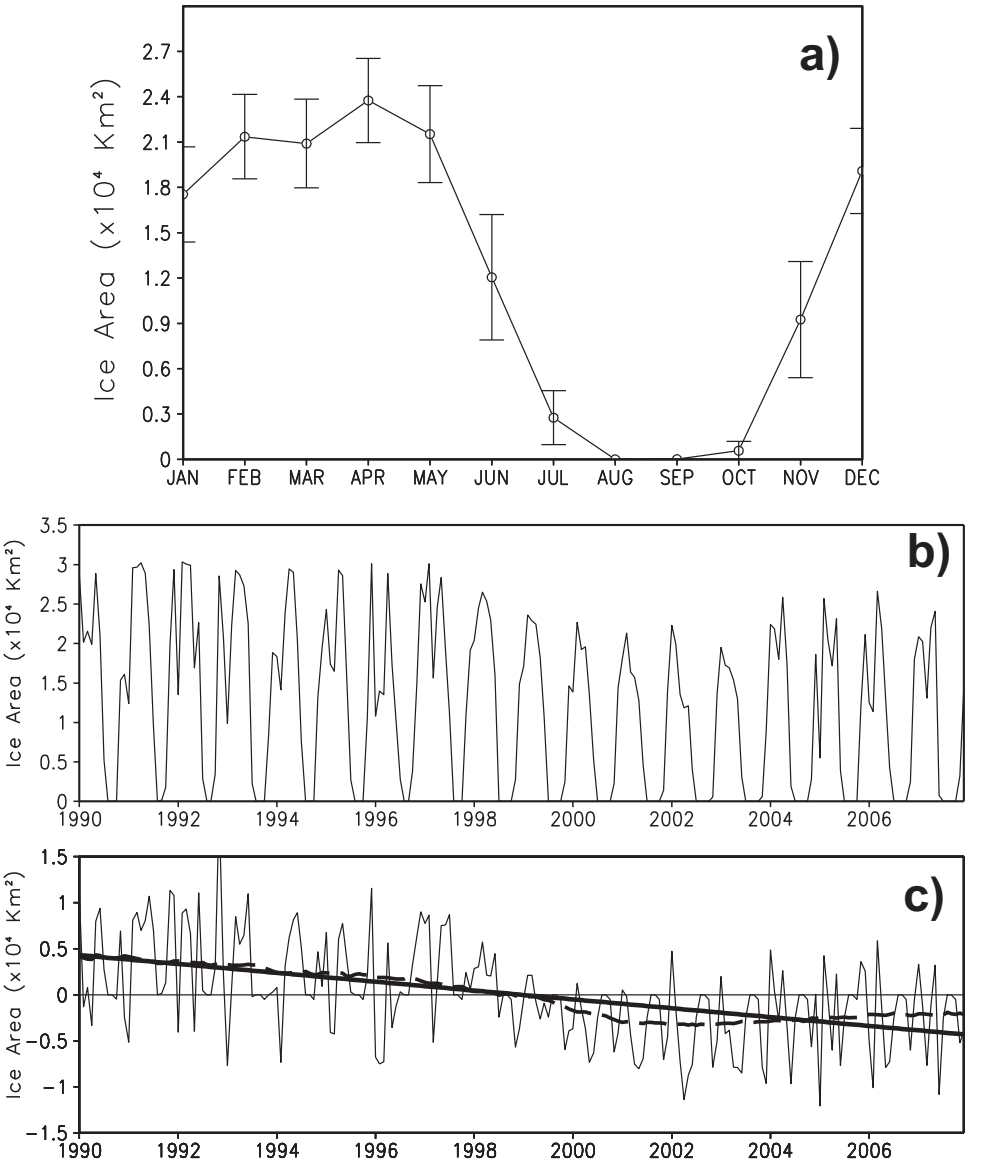

Figure 11. (a) Modeled seasonal climatology of landfast ice area with standard deviations (the vertical bars denote one standard deviation) for the period of 1990–2007; (b) modeled monthly landfast ice area from 1990 to 2007; and (c) modeled monthly landfast ice area anomalies from 1990 to 2007. A 5 year running mean (thick dashed line) and a downward trend (thick solid line) are also given. The linear regression line is presented by Ice Area = 0.4344–0.0040 M, where units are in 10^4 km^2 and M is in months).The landfast ice area is calculated within the Beaufort and Chukchi coastal region between 160°W and 134°W.

positive anomaly along the Beaufort coast (0.1–0.3 m) and Beaufort Sea (0.4–1.2m). Thus indicates that during the melting season, a +DA event significantly reduces landfast ice and pack ice, vice versa during a –DA event.

In November (freezing season), the composite maps were constructed for the +DA (Figure 12c) and –DA (Figure 12d) phases. The concentration difference field (Figure 12g) shows that in the central Beaufort Sea and northern Chukchi Sea, there was positive anomaly of 0.1–0.2, while along the Beaufort coast, a negative anomaly of −0.1 occurred. A similar situation can be seen in the thickness difference field (Figure 12h): a positive thickness anomaly of 0.4–1.2 m occurred between the –DA and +DA in the central Beaufort Sea and in the northern Chukchi Sea. This is difficult to explain in terms of DA forcing. A possible explanation is that the most significant impact of DA on sea ice is its persistency from winter, spring to summer, rather than autumn [*Wang et al.*, 2009a]. Therefore, during the formation season, other factors (such as

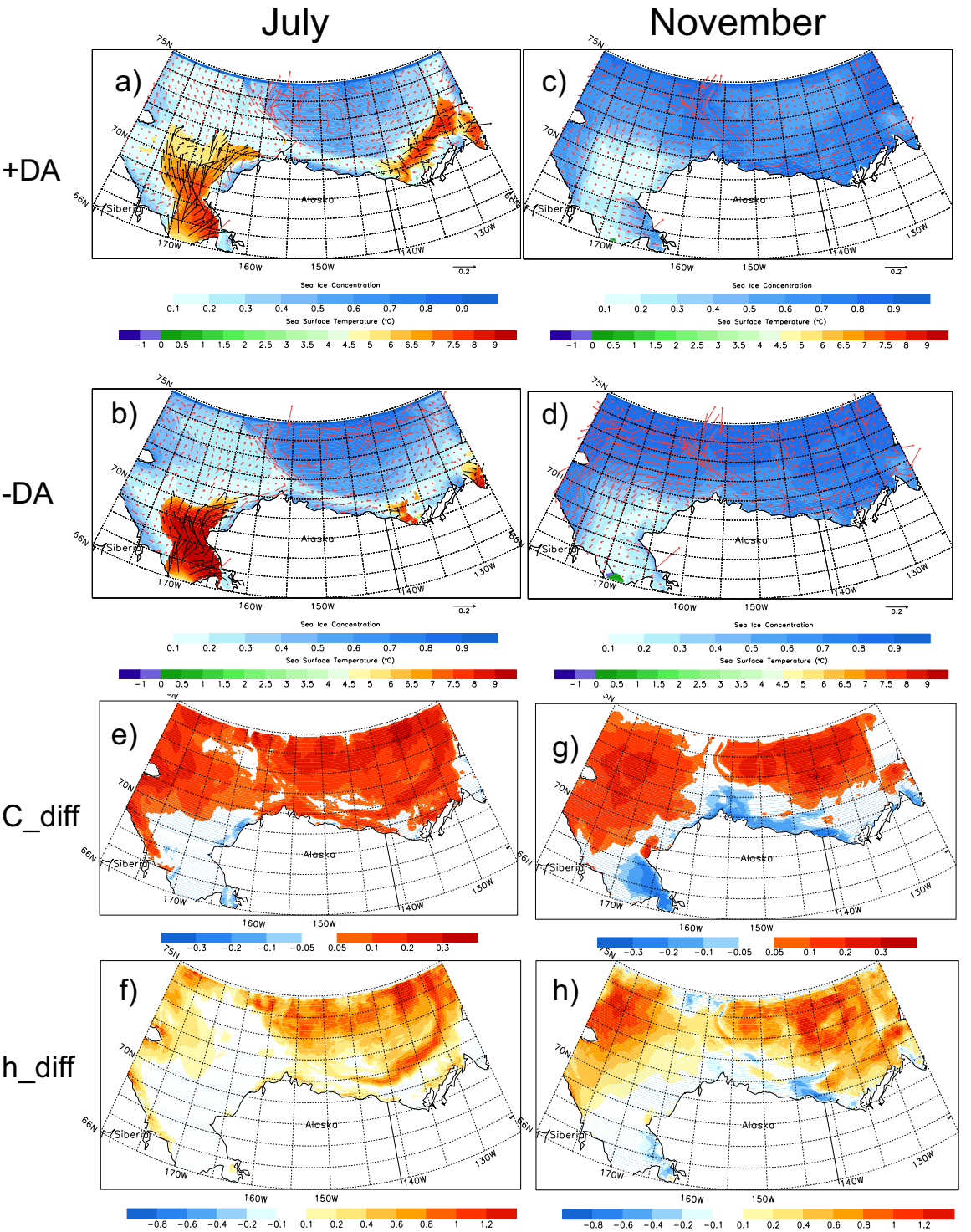

Figure 12. Sea ice cover and ocean circulation in the Beaufort Sea coastal area in July (melting season) and November (freezing season) during +DA and –DA phases, simulated by the CIOM. (a–d) Light to dark blue area shows sea ice concentration between 1 and 10. Red and black arrows indicate sea ice velocity and water velocity (10 m water depth), respectively, and areal colors indicate the SST. (e–h) C_diff (h_diff) denotes the sea ice concentration (thickness) difference between the −DA and +DA composite means. Unit of color bars for concentration (thickness) difference is in tenth (meters).

thermodynamics and the onshore wind derived from the buildup of the Beaufort High that is much stronger than the +DA-derived meridional anomalous (offshore) wind) may play a larger role than the +DA forcing. Therefore, it is inadequate to use DA events to explain the landfast ice formation along the Beaufort

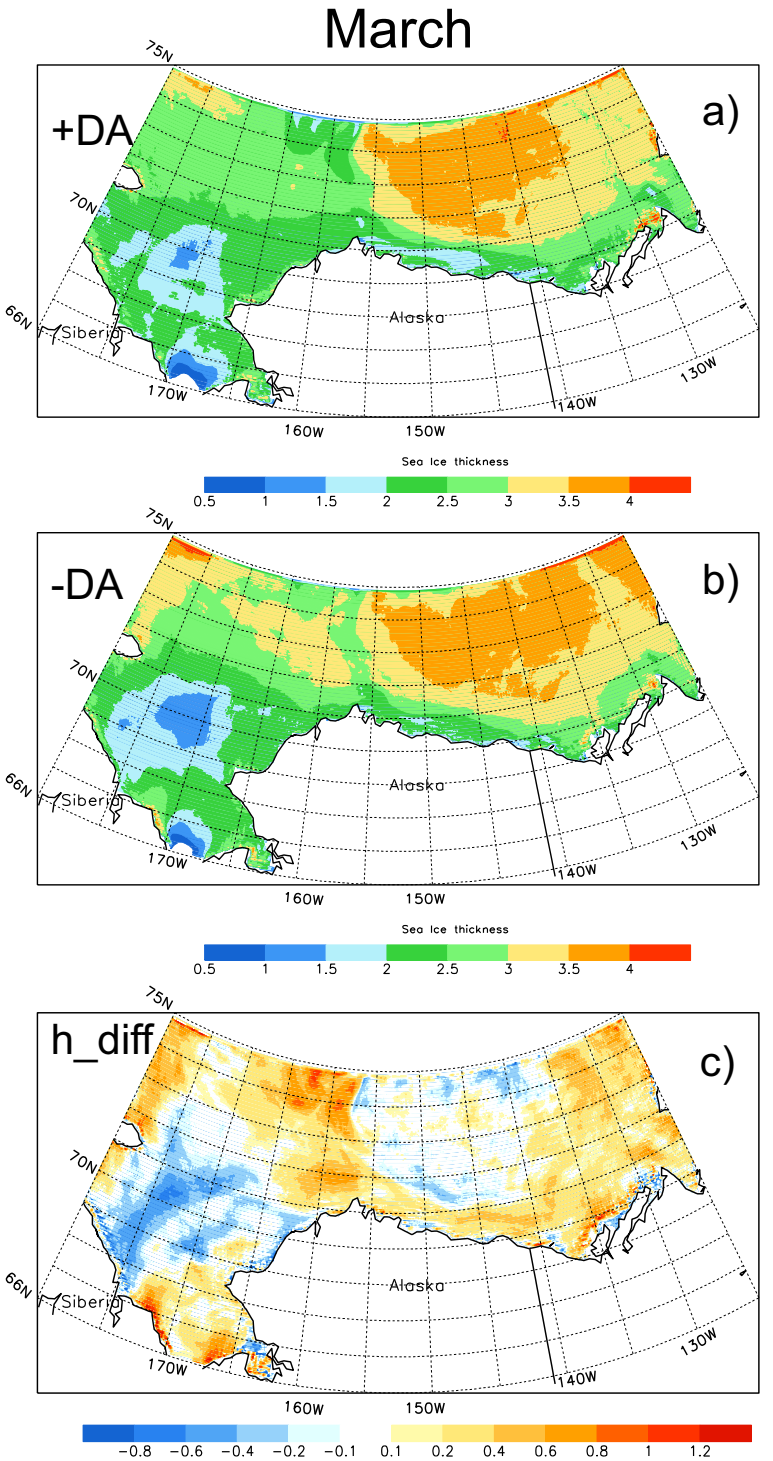

Figure 13. Composite sea-ice thickness (in meters) composite mean in the Beaufort and Chukchi seas in March during (a) +DA and (b) –DA phases, simulated by the CIOM. h_diff denotes the sea-ice thickness difference between the (a) −DA and (b) +DA composite means. Unit of color bars for thickness difference is in meters.

coast during the freezing season, although the DA impact on the pack ice is generally consistent with other seasons.

To examine the impact of DA on winter landfast ice, March ice thickness composite maps were constructed (Figure 13) for the +DA (Figure 13a) and –DA (Figure 13b) phases. During winter season, the Bering Strait

heat transport is negligible or minimal, since the northward transport is minimal and sometime reverses toward the south, and water temperature is near freezing point [*Woodgate et al*., 2010]. The thickness difference field shows a positive anomaly of up to 0.4 m along the Beaufort coast. Large anomaly of up to 0.8 m appeared near the Mackenzie coast and southern Chukchi Sea, while in the central Chukchi Sea, thickness reduced. This indicates that during the +DA (−DA), winter landfast ice along the Beaufort coast reduced (increased). It is noted that because winter sea ice concentration (or extent) cannot change due to the boundary constraint as suggested by *Wang and Ikeda* [2001], it is better to use sea-ice thickness (if available) to capture the ice variability in response to atmospheric forcing.

The Arctic Dipole Anomaly (DA), as defined by the second EOF mode of SLP, has been proven to have more effective impact on driving sea ice out of Arctic (i.e., driving sea ice from the Western Arctic to the East Arctic) than the Arctic Oscillation (AO, the first EOF mode) [*Wu et al*., 2006; *Watanabe et al*., 2006; *Wang et al*., 2009a, 2014]. The key mechanism here is that DA's wind anomaly is meridional, from the Western to the Eastern Arctic (from the East Arctic to the Western Arctic) during positive (negative) phase, while AO's wind anomaly is cyclonic (anticyclonic) during its positive (negative) phase. Thus, the +DA-derived wind anomaly is the offshore (northward) wind along the Chukchi and Beaufort coast, causing more unstable detachment of landfast ice to shore, particularly in the melting seasons.

5. Sensitivity Studies

Wind forcing is the key dynamic forcing to sea ice year round [*Thorndike and Colony*, 1982; *Hu and Wang*, 2010; *Hu et al*., 2011] and is particularly important during the melting and freezing periods due to the interaction of sea ice dynamics with thermodynamics [*Zhang et al*., 2010; *Wang et al*., 2014]. Internal ice advection, i.e., the advection terms in sea ice dynamic equations [*Holland et al*., 1993], in addition to surface water and air temperature advection by ocean circulation and winds [*Hu et al*., 2011], may also be an important factor for sea ice (including landfast ice) formation and decay in the nearshore Beaufort Sea; otherwise, 1-D landfast ice models [*Flato and Brown*, 1996; *König -Beatty and Holland*, 2010] can be used to represent the 2-D ice dynamics and distribution. The warm Bering Strait inflow (boundary forcing) should be important to the nearshore Beaufort Sea ice due to both its dynamics through sea ice advection and thermodynamics through heat transport.

Therefore, a series of sensitivity studies were conducted to investigate sea ice response to changes in these physical processes and forcing. We focus on the mechanisms for landfast ice formation, maintenance, and decay because we are mostly concerned with sea ice variability in the nearshore Beaufort and Chukchi seas, which can potentially impact nearshore oil spill events. The following sensitivity experiments, with year 2002 as control run, were conducted to test the corresponding hypotheses.

1. *No wind forcing during the growth/freezing (September–December) and decay/melting (May–September) periods of landfast ice:* The onshore wind component induced by the anticyclonic Beaufort High pressure is the most important factor to forming landfast ice. Note that the onshore winds impose an opposite forcing to the Pacific-Arctic sea-level pressure head induced Bering Strait inflow [*Woodgate et al*., 2005]. In other words, the onshore winds would slow down the Bering Strait inflow. Thus, without the onshore wind forcing during the formation period, an extreme case of the weakened wind stress, the Bering Strait inflow would be enhanced, and the ACW would spread offshore, joining the BSC, and advect more oceanic heat offshore to the Beaufort Sea (Figure 14c). Thus, pack ice would be reduced in both the melting and growing seasons (Figures 14c and 14d). Without the continuous piling-up of sea ice along the coast by onshore wind-pushing, less landfast ice (Figures 14c and 14d) would exist than the control run (Figures 14a and 14b), consistent with the observation [*Mahoney et al*., 2007a].

There was no pronounced landfast ice anomaly during the melting season (1 August, Figure 14c) that distinguishes it from the control run. The reason is that the BSC is enhanced without the opposite wind forcing and spread offshore, leading to above-normal melting of pack ice, but not landfast ice. However, during the freezing season, without wind forcing, less ice forms along the coast (Figure 14d), because the pile-up process is removed. For example, on 14 November 2002, a freezing season for both landfast ice and pack ice, there was little landfast ice formation along the Beaufort coast (Figure 14d) without the onshore wind forcing derived from the anticyclonic Beaufort High.

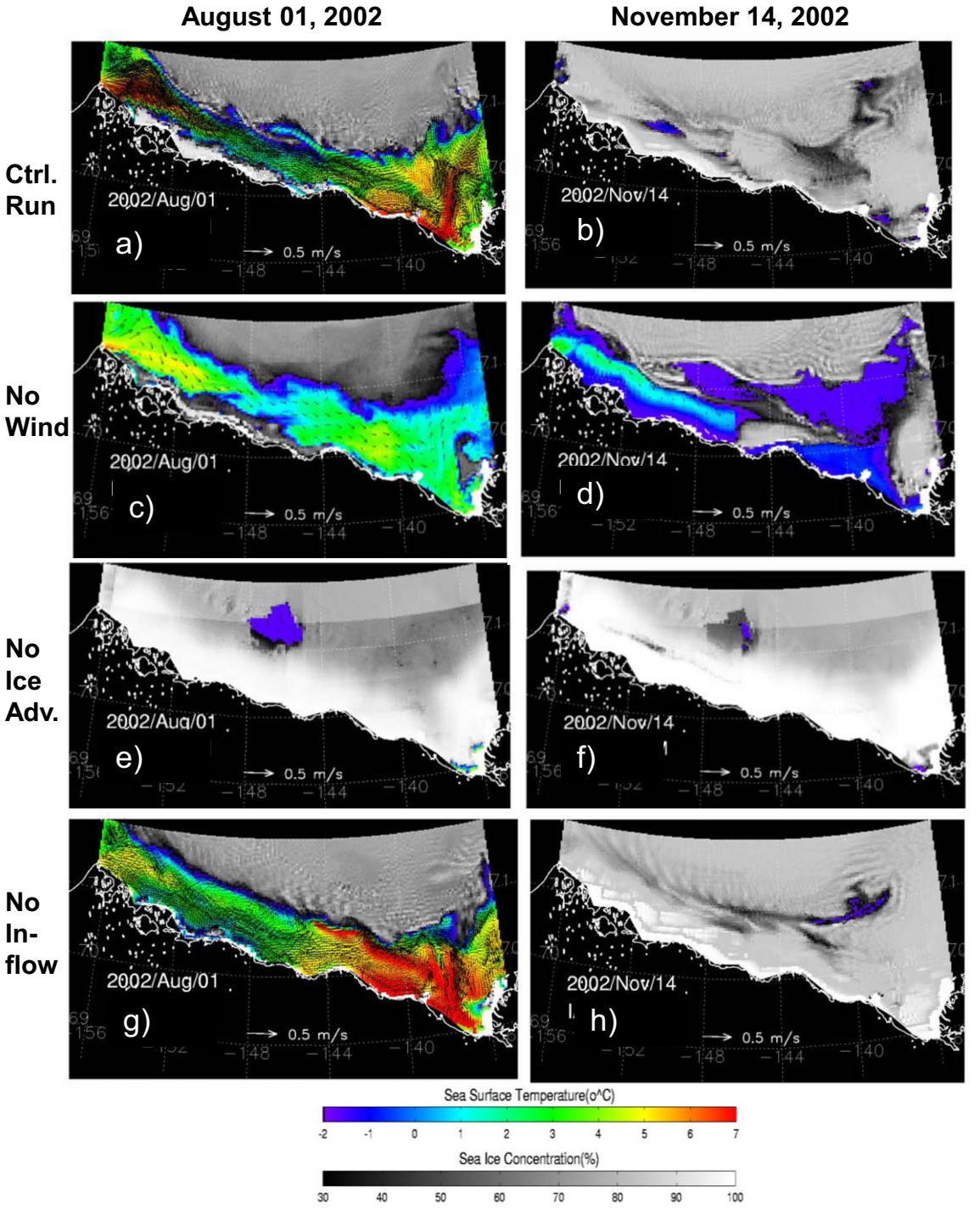

Figure 14. The CIOM-simulated sea ice concentration on (left column) 1 August 2002 and (right column) 14 November 2002 for the (top row) control run that compares sensitivity experiments (1) no wind during the melting season (May–September, second rows), (2) no sea ice advection (third rows), and (3) no Bering Strait inflow (bottom row).

2. *No internal sea ice advection:* We simply turned off the sea ice advection terms in the sea ice dynamic equations to determine if sea ice advection is a key factor, but still under piling-up and ridging effects by wind and surface ocean circulation. Without the internal ice advection, sea ice is controlled only by the thermodynamic process, similar to a 1-D setting [*Flato and Brown*, 1996; *König-Beatty and Holland*, 2010].

Without the sea ice advection (or nonlinear terms), more sea ice and landfast ice exist in the nearshore Beaufort Sea during the melting season (Figure 14e) and during the freezing season (Figure 14f), compared

to the control run (Figures 14a and 14b). Without the ice advection, landfast ice forms faster than the control run. This indicates that sea ice formation and decay controlled only by the thermodynamic process cannot reproduce open water along the Alaskan Beaufort coast. Thus, the sea ice advection process is very important. This also implies that model parameters derived from any 1-D thermodynamic ice models may not be suitable for 2-D thermodynamic and dynamic sea-ice models. Therefore, special caution should be taken in using parameters of an ice model when transferring a 1-D ice thermodynamic model to a 2-D thermodynamic and dynamic model.

3. *No Bering Strait inflow:* We simply zeroed the Bering Strait inflow to investigate the Bering Strait inflow impact on landfast ice in the Beaufort and Chukchi seas. The inflow advects the warm Bering water (i.e., transport heat) to the Chukchi Sea [*Woodgate et al*., 2005, 2010; *Weingartner et al*., 2005] and enhances both bottom and lateral melting [*Ohshima and Nihashi*, 2005] all the way to the Beaufort Sea.

Thus, without this inflow, the coastal-trapped current is significantly weakened and thus, the pile-up process by the right-pointing Coriolis force would be reduced. This is why less landfast ice would stay along the Beaufort coast during the melting season (1 August, Figure 14g). It is noted that the Bering Strait inflow separates into three branches: Herald Canyon, Central Channel, and Alaska Coastal Water (ACW). The majority of the volume and heat transport is through the first two channels, and turns to the right to join the Beaufort Slope Current (BSC) (see Figure 1) [*Winsor and Chapman*, 2004; *Pickart*, 2004, *Pickart et al*., 2009; *Woodgate et al*., 2005], while the ACW drainages into the Barrow Canyon, and then joins the BSC [*Shimada et al*., 2006; *Pickart*, 2004; *Watanabe*, 2011]. Therefore, it is understandable that the landfast ice at shore (less than 35m) is less affected by the inflow heat transport in the melting season. The melting season is several months before the maximum warm Bering Strait inflow moves in (with a maximum being in summer). Therefore, the local melting dominates, in particular, near the Mackenzie Delta where the SST is higher than that in the Barrow Canyon area. Nevertheless, in the control run, both the Barrow Canyon area and Mackenzie Delta experience high SST, because in the former, oceanic heating is advected from the Bering Strait inflow.

In contrast, there is more pronounced impact on sea ice without this inflow during the freezing season. Due to no heat transport along the BSC year round, the heat content should be low-than-normal in the nearshore Beaufort Sea; so there is more pack ice and then more landfast ice in the freezing season. In other words, if the Bering Strait inflow reduces in the summer season, it would have little impact on the landfast ice in the earlier melting season, but significant impact (increase in landfast ice) during the coming freezing season. The freezing process is enhanced (Figure 13h) because the local cooling dominates thermodynamically in the relatively shallow shelf compared to the advection, while local winds dominate dynamically, leading to enhanced onshore piling-up process [*Mahoney et al*., 2007b].

In summary, wind forcing, ice advection, and Bering Strait inflow all are important to landfast ice formation and decay, and melting along the Beaufort coast, compared to the control run. During the melting season when the advected ocean heat transport increases, all the factors are involved, leading to very complex interaction between the dynamics and thermodynamics. In contrast, during the freezing season when the oceanic heat flux advection is weakened, the local cooling and wind forcing dominate the landfast ice formation.

6. Conclusions and Discussion

The 3.8 km CIOM was successfully applied to the Chukchi and Beaufort seas to conduct realistic simulations that were compared to available ship surveys and satellite measurements. Based on the above investigations including the sensitivity studies, the following major conclusions can be drawn:

1. The Chukchi-Beaufort seas coastal current was well reproduced, which consists of the ACW, the Central Channel, and the Herald Valley branches. The ESC was also captured with a cold and fresh water mass. The ocean circulation, such as the Beaufort Gyre and the imbedded small mesoscale eddies with anticyclones outnumbering cyclones along with the seasonal cycle were very well simulated. The previous theory can be used to explain why there are small mesoscale eddies at the negatively sloping bottom in the nearshore Chukchi and Beaufort coasts.

2. The seasonal cycle of sea ice was well reproduced with the lateral melting parameterization. Landfast ice, for the first time, was reproduced under daily atmospheric forcing without anchoring mechanism. The simulated landfast ice compares reasonably well with the synthetic aperture radar measurements. Seasonal cycle of landfast ice was derived with the largest standard deviations (changes) occurring in the melting (June) and formation (November) seasons.

3. Interannual variability of landfast ice was also simulated from 1990 to 2008. It was found that before and after 1998, there was significant change in seasonality, with longer duration prior to 1998 than after 1998. Consequently, there was a positive (negative) anomaly in landfast ice area before (after) 1998. This regime shift in 1998, known as a strong El Nino event, should be validated using historical data. A composite analysis shows that during the +DA phase, there was less landfast ice possibly due to (1) anomalous northward or offshore wind along the Beaufort coast and (2) anomalous northward oceanic and atmospheric heat transports into the Chukchi and Beaufort coasts from the south, melting more sea ice during the melting season. During the –DA phase, an opposite scenario occurred, leading to more pack and landfast ice from winter to the melting season due to (1) anomalous southward (onshore) wind and (2) anomalously low northward oceanic and atmospheric heat transport into the Chukchi and Beaufort seas. Nevertheless, during the formation season (autumn), DA's impact on landfast ice along the Beaufort coast is not significant, since other factors may dominate the formation process.

4. Sensitivity experiments suggest that the most important factors affecting pack ice and landfast ice are wind associated with the Beaufort High, the Bering Strait inflow, and sea ice advection. Onshore winds can pile up ice toward shore, while offshore wind can destabilize and detach landfast ice from the shore [*Mahoney et al*., 2007b]. Of course, a high resolution model resolving the topography and geometry is a necessary configuration, since landfast ice is naturally attached to the complex geometry.

It should be noted that this study attempts to investigate nearshore landfast ice using the existing CIOM that does not have anchoring dynamics. In other words, the simulated landfast ice may actually move, but at a very small speed. The actual landfast ice is anchored to the bottom or attached to shore in the winter with negligible speed, and starts to move during the melting and formation seasons. Through this study with "landfast ice" loosely defined, we can see that the CIOM (and other coupled ice-ocean models) has the capability to simulate the nearshore thermodynamics and dynamics of sea ice, with a lack of an anchoring mechanism. Therefore, anchoring dynamics of landfast ice is emerging as a research topic for the Arctic community to better simulate and forecast sea ice in nearshore ice-covered seas.

Tidal forcing should be important in nearshore sea ice dynamics including landfast ice, in particular during breakup and breeze-up periods. So far, few coupled ice-ocean models include tidal forcing, which needs to be addressed in the near future. A suite of ice model parameters and parameterizations associated with tidal forcing should be investigated since they may differ in magnitude in the absence of tides.

Appendix A: Model Description

This coupled ice-ocean model was described in great detail in the model development and application to the pan-Arctic region [*Wang et al*., 2002]. In the following, we only describe the parts necessary for the completeness of this report.

A1. Sea-Ice Model

The sea ice component of the coupled model is a thermodynamic model based on multiple categories of ice thickness distribution function [*Thorndike et al*., 1975; *Hibler*, 1980] and a dynamic model based on a viscous-plastic sea ice rheology [*Hibler*, 1979].

The evolution of the thickness distribution function satisfies a continuity equation

$$\frac{\partial g}{\partial t}+\nabla\cdot(\vec{V}_g)=-\frac{fg}{\partial h}+\psi \tag{A1}$$

where $\vec{V}$ is velocity vector (*u, v*), ***f(h)*** is the thermodynamic vertical growth rate of ice, ***g*** is the sea-ice thickness distribution function, and ***g(h)dh*** is defined as the fraction of area covered by the ice with thickness between ***h*** and ***h*** + ***dh***. The averaged thickness $\overline{h}$ and concentration ***A*** of sea ice in a grid is expressed from **g(*h*)** as

$$\boldsymbol{A}=\int_{0+}^{h}\boldsymbol{g}(\boldsymbol{h})\boldsymbol{dh} \tag{A2}$$

and

$$\overline{\boldsymbol{h}}=\int_{0}^{h}\boldsymbol{g}(\boldsymbol{h})\boldsymbol{h}\boldsymbol{dh} \tag{A3}$$

ψ is the mechanical redistribution function, which represents the creation of open water and ridging during ice deformation. The redistribution process conserves ice volume. The redistribution function is parameterized as described by *Yao et al*. [2000]. The vertical growth rate $\boldsymbol{f(h)}$ of ice thickness is determined by the ice thermodynamics.

The model thermodynamic interactions between ice, ocean, and atmosphere are shown in Figure 15. The heat budget on the upper ice surface is

$$\boldsymbol{Q}_{\mathbf{AI}}=\boldsymbol{Q}_{\mathbf{Si}}+\boldsymbol{Q}_{\mathbf{Ei}}+\boldsymbol{Q}_{\mathbf{L}}+(\mathbf{1}-\alpha_{\mathbf{i}})\boldsymbol{I}_{\mathbf{0}}-\varepsilon_{\mathbf{i}}\sigma\boldsymbol{T}_{0}^{4} \tag{A4}$$

where $\alpha_{\mathbf{i}}$ is the albedo of sea ice (0.75 during the freezing period from October to March, 0.65 during the melting period from April to September). When snow exists, ice albedo is replaced by the snow albedo α_S (0.9); $\varepsilon_{\mathbf{i}}$ is the emissivity of ice. $\boldsymbol{I}_{\mathbf{0}}$ is the short wave solar radiation reaching the ice surface; $\boldsymbol{Q}_{\boldsymbol{Si}}$, $\boldsymbol{Q}_{\boldsymbol{Ei}}$, and $\boldsymbol{Q}_{\boldsymbol{L}}$ are the sensible heat flux, the latent heat flux, and the effective longwave radiation flux from ice surface, respectively. $\boldsymbol{Q}_{\mathbf{Si}}$, $\boldsymbol{Q}_{\mathbf{Ei}}$, and $\boldsymbol{Q}_{\mathbf{L}}$ are parameterized by the following formulae,

$$\boldsymbol{Q}_{\mathbf{Si}}=\rho_{\mathbf{a}}\boldsymbol{C}_{\mathbf{p}}\boldsymbol{Cs}|\overrightarrow{V}_{a}|(\boldsymbol{T}_{\mathbf{a}}-\boldsymbol{T}_{0}) \tag{A5}$$

$$\boldsymbol{Q}_{\mathbf{Ei}}=\rho_{\mathbf{a}}\boldsymbol{LeCe}|\overrightarrow{V}_{a}|(\boldsymbol{q}_{\mathbf{a}}-\boldsymbol{q}_{0}) \tag{A6}$$

$$\boldsymbol{Q}_{\mathbf{L}}=\varepsilon_{\mathbf{a}}\sigma[1-\boldsymbol{k}_{\mathbf{c}}\boldsymbol{C}_{\mathbf{L}}](\mathbf{a}-\mathbf{b}\sqrt{e_a})\boldsymbol{T}_{\mathbf{a}}+4(\boldsymbol{T}_{0}-\boldsymbol{T}_{\mathbf{a}})\boldsymbol{T}_{\mathbf{a}}^{3} \tag{A7}$$

where $\boldsymbol{q}_{\mathbf{a}}$ and $\boldsymbol{T}_{\mathbf{a}}$ are the specific humidity and air temperature of air; $\boldsymbol{q}_{\mathbf{0}}$ is the saturated specific humidity on ice; $\boldsymbol{T}_{\mathbf{0}}$ is the surface ice temperature; e_a is the atmospheric vapor pressure. $\boldsymbol{C}_{\mathbf{p}}$ is the specific heat of air at constant pressure. $\boldsymbol{Le}$ is the latent heat sublimation on the ice surface. $\boldsymbol{Cs}$ and $\boldsymbol{Ce}$ are the sensible heat and latent heat bulk transfer coefficients, respectively. $\varepsilon_{\mathbf{a}}$ is the emissivity of air. σ is Stefan-Boltzmann constant. $\boldsymbol{k}_{\mathbf{c}}$ is the cloud factor, and $\boldsymbol{C}_{\mathbf{L}}$ is the cloud fraction. $\boldsymbol{T}_{\mathbf{a}}$ (in Kelvin) is the air temperature, $\boldsymbol{a}$ and $\boldsymbol{b}$ are empirical constants ($a = 0.254$, $b = 4.95 \times 10^{-3}$). The surface ice temperature $\boldsymbol{T}_{\mathbf{0}}$ is determined from the surface heat balance equation,

$$\boldsymbol{Q}_{\mathbf{AI}}-\boldsymbol{Q}_{\mathbf{c}}=\mathbf{0} \tag{A8}$$

where $\boldsymbol{Q}_{\mathbf{c}}$ is the internal conductive heat flux through ice. A linear ice temperature profile and a constant thermal conductive coefficient $\boldsymbol{k}_{\mathbf{i}}$ are used in this study. Thus, for the ice category with thickness $\boldsymbol{h}$,

$$\boldsymbol{Q}_{\mathbf{c}}=-\boldsymbol{k}_{\mathbf{i}}(\boldsymbol{T}_{0}-\boldsymbol{T}_{\boldsymbol{f}})/\mathbf{h} \tag{A9}$$

where T_f is the freezing temperature of seawater on bottom ice surface, which is a function of the salinity of seawater ($=-0.0544S_0 + 273.15K$, where S_0 is the salinity of upmost ocean grid, in practical salinity unit, psu). For the snow-covered ice, the conductive coefficient will be replaced by $\frac{\boldsymbol{k}_{\boldsymbol{i}}\boldsymbol{k}_{\boldsymbol{s}}}{\boldsymbol{h}\boldsymbol{k}_{\boldsymbol{s}}+\boldsymbol{h}_{\boldsymbol{s}}\boldsymbol{k}_{\boldsymbol{i}}}$, where $\boldsymbol{h}_{\mathbf{s}}$ is the snow depth.

If the calculated $\boldsymbol{T}_{\boldsymbol{0}}$ is found to be over 0°C, it is forced to be 0°C. The extra heat of equation (A8) is used to melt the ice at the upper surface, and the melted water will drain to the ocean immediately. The volume flux of melting water $\boldsymbol{W}_{\boldsymbol{AI}}$ is

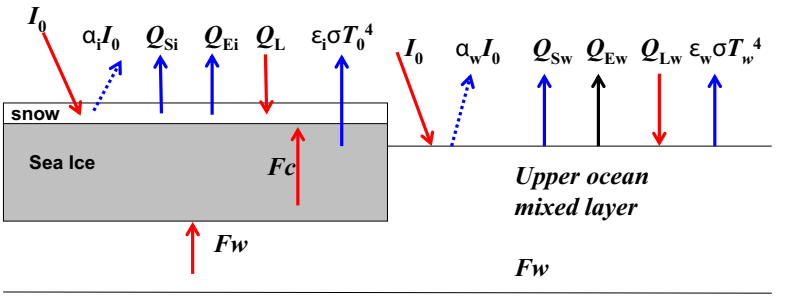

Figure 15. Heat budget between the ocean and sea ice.

$$W_{AI} = [Q_{AI} - Q_c]/L \tag{A10}$$

The growth rate at the bottom of the sea ice is

$$W_{IW} = [Q_c - F_T]/L \tag{A11}$$

where L is the volume latent heat of fusion and F_T is the oceanic heat flux out of the ocean surface (assumed to be uniform over a model grid cell). Thus, the growth rate $f(h)$ for sea ice with thickness h is the sum of (A10) and (A11), i.e.

$$f(h) = [Q_{AI} - F_T]/L \tag{A12}$$

For the open water in the ice zone, the growth rate of sea ice is

$$W_{AW} = [Q_{AW} - F_T]/L \tag{A13}$$

where Q_{AW} is the heat budget between the atmosphere-ocean interface, excluding the solar radiation that is absorbed in the water column. Q_{AW} is calculated using a similar parameterization to (A4) but without the solar radiation terms, i.e.,

$$Q_{AW} = Q_{SW} + Q_{EW} + Q_{LW} - \varepsilon_w \sigma T_w^4 \tag{A14}$$

where ε_w is the emissivity of water. T_w is the sea surface temperature (SST). Q_{Sw}, Q_{Ew}, and Q_L are the sensible heat flux, the latent heat flux, and the effective longwave radiation flux from water surface, which are parameterized similar to (A5)–(A7). When the W_{AW} is negative, the "melting" of ice to water is implied. In this case, the equivalent heat is redistributed to melt the remaining ice. The total ice growth rate is integral over various ice thicknesses with weight $g(h)$.

The ice velocity $\vec{V}$ (u_I, v_I) is determined from the momentum equation

$$m\frac{d\vec{V}}{dt} + mf\vec{k} \times \vec{V} = -mg\nabla H + \vec{\tau}_a - \vec{\tau}_w + \vec{F} \tag{A15}$$

or in terms of scalar format,

$$\frac{\partial u_I}{\partial t} + u_I\frac{\partial u_I}{\partial x} + v_I\frac{\partial u_I}{\partial y} - fv_I = -g\frac{\partial H}{\partial x} + \frac{\tau_{ax}}{\rho_I} - \frac{\tau_{Wx}}{\rho_I} + \frac{F_x}{\rho_I}$$
$$\frac{\partial v_I}{\partial t} + u_I\frac{\partial v_I}{\partial x} + v_I\frac{\partial v_I}{\partial y} - fu_I = -g\frac{\partial H}{\partial x} + \frac{\tau_{ay}}{\rho_I} - \frac{\tau_{Wy}}{\rho_I} + \frac{F_y}{\rho_I}$$

where f is the Coriolis parameter and m is the ice mass in a grid. ∇H is the gradient of sea surface elevation, $\vec{F}$ is the internal stresses [see *Hibler*, 1979; *Wang et al.*, 1994], and $\vec{\tau}_a$ and $\vec{\tau}_w$ are the air and water stresses, respectively. They are determined by the bulk formulae

$$\vec{\tau}_a = \rho_a C_a |\vec{V}_a| \vec{V}_a \tag{A16}$$

$$\vec{\tau}_w = \rho_w C_w |\vec{V}_w - \vec{V}_i| (\vec{V}_w - \vec{V}_i) \tag{A17}$$

where $\vec{V}_a$ is the wind velocity vector. $\vec{V}_w$ is the current velocity vector of the upmost ocean layer. C_a (=1.2 $\times 10^{-3}$) and C_w (=5.5 $\times 10^{-3}$) are the bulk coefficients of wind stress and water stress, respectively. ρ_a is the air density and ρ_w is the seawater density. $\vec{F}$ is the two-dimensional internal ice stress tensor, which is derived from the viscous plastic rheology with elliptical yield curve rate $e = 2$ of *Hibler* [1979] and involves a compressive ice strength

$$P = P^* \bar{h} \exp[-C(1-A)] \tag{A18}$$

where P^* and C are empirical constants (here 2.5 $\times 10^4$ N m^{-2} and 20, respectively). e is the ratio of principal axes of the ellipse, P^* is the ice strength, and C is the ice strength decay constant. This formulation requires that the ice strength strongly depends on the amount of thin ice, characterized by $(1 - A)$, which also allows the ice to strengthen as it becomes thicker, as measured by thickness $\bar{h}$. The redistribution function is parameterized as described by *Thorndike et al*. [1975] and *Yao et al*. [2000], differing from the treatment by *Hibler* [1980], who used a given thickness to ridged ice of a single thickness (the multiplication factor is chosen as 15). Table 2 lists the parameters, their values and units that are used in this model.

In this sea-ice model, we introduced a thermodynamical process: lateral melting, which relates to a variable of the bulk heat transfer coefficient, K_b, depending on wind speed proposed by *Ohshima and Nihashi* [2005] add to references.

$$K_b = C_h u_* \tag{A19}$$

$$u_* = \sqrt{C_d} u_{rel} \tag{A20}$$

where C_h and u_* are the heat transfer coefficient and friction velocity, respectively. u_* is derived from (A20) using drag coefficient C_d and relative velocity u_{rel} (1% of geostrophic wind velocity). The melting resulting from heat input by wind is expressed as

$$\frac{dC}{dt} = \frac{C_w \rho_w K_b C (T_0 - T_f)}{L \rho_i h_0} \tag{A21}$$

Note that the lateral melting is about twice as large as bottom melting during the melting season. The parameters used in the CIOM along with their units are listed in Table 2.

A2. Ocean Model

The Princeton Ocean Model [*Blumberg and Mellor*, 1987; *Mellor*, 2004] is used as the ocean component of the coupled mode in this study. The model has a free surface, uses sigma coordinates in the vertical, and employs a mode-split technique. The model embeds a second-order turbulence closure submodel. Smagorinsky diffusivity along sigma surfaces is employed in the horizontal diffusion.

The governing equations of ocean dynamics in Cartesian-coordinate are as follows:

$$\frac{\partial u}{\partial t} + u\frac{\partial u}{\partial x} + v\frac{\partial v}{\partial y} + w\frac{\partial u}{\partial z} - fv = -g\frac{\partial \eta}{\partial x} + \frac{\partial}{\partial x}\left(A_H \frac{\partial u}{\partial x}\right) + \frac{\partial}{\partial y}\left(A_H \frac{\partial u}{\partial y}\right) + \frac{\partial}{\partial z}\left(A_z \frac{\partial u}{\partial z}\right)$$

$$\frac{\partial v}{\partial t} + u\frac{\partial v}{\partial x} + v\frac{\partial v}{\partial y} + w\frac{\partial v}{\partial z} - fu = -g\frac{\partial \eta}{\partial y} + \frac{\partial}{\partial x}\left(A_H \frac{\partial v}{\partial x}\right) + \frac{\partial}{\partial y}\left(A_H \frac{\partial v}{\partial y}\right) + \frac{\partial}{\partial z}\left(A_z \frac{\partial v}{\partial z}\right)$$

$$\frac{\partial u}{\partial x} + \frac{\partial v}{\partial y} + \frac{\partial w}{\partial z} = 0$$

The temperature and salt equations in sigma-coordinates are

Table 2. Constants Used in CIOM[a]

Symbols	Description	Values	Units
a	Empirical constant	0.254	
b	Empirical constant	4.95×10^{-3}	
α_i	Albedo of sea ice	0.65–0.75	
α_S	Albedo of snow	0.9	
α_w	Albedo of sea water	0.1	
C	Ice decay constant	20	
C_a	Wind stress bulk coefficient	1.2×10^{-3}	
C_w	Water stress bulk coefficient	5.5×10^{-3}	
C_e	Latent heat bulk transfer coefficient	1.75×10^{-3}	
C_S	Sensible heat bulk transfer coefficient	2.32×10^{-3} when Ts < Ta 1.75×10^{-3} when Ts ≥Ta	
C_P	Specific heat of air	1410	J $kg^{-1}K^{-1}$
$C_{P,W}$	Specific heat of sea water	3903	J $kg^{-1}K^{-1}$
e	Yield curve eccentricity	2	
e_i	Emission of sea ice	0.65–0.75	
L	Volume latent heat of fusion		
L_e	Latent heat sublimation on ice surface	3.32×10^{-3}	J kg^{-1}
k	von Karman constant	0.4	
K_C	Cloud factor	0.62	
k_i	Thermal conductive coefficient	2.04	
P^*	Ice strength	2.5×10^4	Nm^{-2}
Pr	Molecular Prantl number	12.9	
ρ_a	Air density	1.3	kg m^{-3}
ρ_i	Sea ice density	910	kg m^{-3}
ρ_w	Seawater density	1025	kg m^{-3}
S_I	Sea ice salinity	5 psu	
Sc	Schmidt number	2432	
σ	Stefan-Boltzmann constant	5.67×10^{-8}	
$\Delta x = \Delta y$	Model horizontal grid size	3800	m
ΔT	Time step for eternal mode	20	s
Δt	Time step for internal mode and ice 400	s	

[a]Temperature is in Kelvin, °K, 0°C = 273.15°K.

$$\frac{\partial T}{\partial t} + \nabla \cdot (\vec{V}_w S) + \frac{\partial \omega T}{\partial \sigma} = \frac{\partial}{\partial \sigma} + \left(K_H \frac{\partial T}{\partial \sigma} \right) + F_T - (1 - \alpha_w) \frac{\partial I_0}{\partial \sigma} \tag{A22}$$

$$\frac{\partial S}{\partial t} + \nabla \cdot (\vec{V}_w S) + \frac{\partial \omega S}{\partial \sigma} = \frac{\partial}{\partial \sigma} + \left(K_H \frac{\partial S}{\partial \sigma} \right) + F_S \tag{A23}$$

and the surface heat flux is

$$\boldsymbol{Q_{AW} = Q_{Sw} + Q_{Sw} + Q_{Lw} - \varepsilon_w \sigma T_w^4} \tag{A24}$$

in the ice-free grid cell, and

$$\boldsymbol{A F_T + (1 - A) Q_{AW}} \tag{A25}$$

in the ice-covered grid cell.

A3. Ice-Ocean Coupling

Heat and salt fluxes at the ice-ocean interface are governed by the boundary processes as discussed by *Mellor and Kantha* [1989]. The new level 2.5 closure turbulence model is employed according to *Kantha and Clayson* [1994]. In grid cells in which ice is present, the heat flux out of the ocean is

$$\boldsymbol{F_T = -\rho_w C_p C_{Tz} (T_f - T)} \tag{A26}$$

where $\boldsymbol{C_p}$ is the specific heat of seawater and $\boldsymbol{T}$ is the ocean temperature at the uppermost model grid (in our model the midpoint of the uppermost ocean layer). The heat transfer coefficient $\boldsymbol{C_{Tz}}$ is given by

$$C_{Tz} = \frac{u_*}{P_{rt}\ln(-z/z_0)/k + B_T}$$
$$B_T = b(z_0 u_*/\nu)^{1/2} P_r^{2/3} \quad \text{(A27)}$$

where u_* is the friction velocity, P_{rt} is a turbulent Prantl number, z is the vertical coordinate corresponding to the temperature T, z_0 is the roughness length, and k is the von Karman constant. The molecular sublayer correction is represented by B_T, where P_r is a molecular Prantl number, ν is the kinematic viscosity, and b is an empirical constant (=3). The salt flux out of the ocean is

$$F_S = (W_{AI} + W_{IW} + W_{AW})(S_I - S) + (1 - A)S(P - E) \quad \text{(A28)}$$

where S_I is the salinity of ice (=5 psu), S is the salinity at the uppermost model grid point, and $(P-E)$ is the volume flux of precipitation minus evaporation.

Analogous to the heat flux (A26), the salt flux is defined as

$$F_S = -C_{Sz}(S_0 - S) \quad \text{(A29)}$$

where S_0 is the salinity at the ice-ocean interface. The salt transfer coefficient C_{Sz} is

$$C_{Sz} = \frac{u_*}{P_{rt}\ln(-z/z_0)/k + B_S}$$
$$B_S = b(z_0 u_*/\nu)^{1/2} Sc^{2/3} \quad \text{(A30)}$$

where Sc is the Schmidt number. Since Sc =2432, and P_r=12.9, and $C_{Tz} > C_{Sz}$, this can lead to the production of frazil ice in the water column as discussed by *Mellor and Kantha* [1989]. Frazil ice is immediately added to the floating ice.

The ice-water stress is

$$\tau_w/\rho_w = \frac{k u_*}{\ln(z/z_0)}(\vec{V}_i - \vec{V}_w)$$

where $\vec{V}_w$ is the ocean velocity vector at the uppermost model grid.

Acknowledgments
We sincerely thank the University of Alaska Coastal Marine Institute (CMI) and Minerals Management Service (MMS) for the support. Thanks also go to R. Prentki, Ron Lai, and Caryn Smith of BOEM for their discussion and input. The NSF support of this collaborative research was acknowledged: ARC-0712673 to H. Eicken and J. Wang, and ARC-0714078 to Y. Yu. This study is also supported by the NOAA CPO Office of Arctic Research through RUSALCA project. We appreciate very much three anonymous reviewers for providing valuable and constructive comments that help significantly improve the presentation of the paper. Editorial work by Cathy Darnell is also appreciated. This is GLERL contribution 1710.

References

Blumberg, A. F., and G. L. Mellor (1987), A description of 3-D coastal ocean circulation model, in *Coastal and Estuarine Sciences 4: 3-D Coastal Ocean Models*, edited by N. S. Heaps, pp. 1–16, AGU, Washington, D. C.

Cavalieri, D., P. Gloersen, and J. Zwally (1990), DMSP SSM/I daily and monthly polar gridded sea ice concentrations [1 Jan 1990 to 31 Dec 2006], edited by J. Maslanik and J. Stroeve, Natl. Snow and Ice Data Cent., Digital Media, Boulder, Colo.

Chao, S.-Y., and P.-T. Shaw (2002), A numerical investigation of slanted convection and subsurface anticyclone generation in an Arctic baroclinic current system, *J. Geophys. Res.*, *107*(C3), 3019, doi:10.1029/2001JC000786.

Chen, C., G. Gao, J. Qi, A. Proshutinsky, R. C. Beardsley, Z. Kowalik, H. Lin, and G. Cowles (2009), A new high-resolution unstructured grid finite volume Arctic Ocean model (AO-FVCOM): An application for tidal studies, *J. Geophys. Res.*, *114*, C08017, doi:10.1029/2008JC004941.

Clement, J. L., W. Maslowski, L. W. Cooper, J. M. Grebmeier, and W. Walczowski (2005), Ocean circulation and exchanges through the northern Bering Sea-1979–2001 model results, *Deep Sea Res., Part II*, *52*, 3509–3540.

Comiso, J. (1990), DMSP SSM/I daily and monthly polar gridded sea ice concentrations, edited by J. Maslanik and J. Stroeve, Natl. Snow and Ice Data Cent., Boulder, Colo., Digital Media.

Eicken, H., L. H. Shapiro, A. G. Gaylord, A. Mahoney, and P. W. Cotter (2005), *Mapping and Characterization of Recurring Spring Leads and Landfast Ice in the Beaufort and Chukchi Seas*, 141 pp., U.S. Dep. of Inter., Miner. Manage. Serv., Alaska Outer Cont. Shelf Reg., Anchorage.

Flato, G. M., and R. D. Brown (1996), Variability and climate sensitivity of landfast Arctic sea ice, *J. Geophys. Res.*, *101*, 25,767–25,777, doi:10.1029/96JC02431.

Fu, G., K. S. Baith, and C. R. McClain (1998), SeaDAS: The SeaWiFS data analysis system, paper presented at The 4th Pacific Ocean Remote Sensing Conference, Qingdao, China, 28–31 Jul.

Griffiths, C., M. Ikeda, and P. C. Smith (2000), A numerical model comparison of baroclinic instability in the presence of topography, *Tellus, Ser. A*, *52*, 42–65.

Haapala, J., H. E. M. Meier, and J. Rinne (2001), Numerical investigations of future ice conditions in the Baltic Sea, *Ambio*, *30*(4–5), 237–244.

Hart, J. E., and P. D. Killworth (1976), On open ocean baroclinic instability in the Arctic, *Deep Sea Res. Oceanogr. Abstr.*, *23*(7), 637–645.

Hibler, W. D., III (1979), A dynamic and thermodynamic sea ice model, *J. Phys. Oceanogr.*, *9*, 15,959–15,969.

Hibler, W. D., III (1980), Modeling a variable thickness sea ice cover, *Mon. Weather Rev.*, *108*, 1943–1973.

Holland, D. M., L. A. Mysak, D. K. Manak, and J. M. Oberhuber (1993), Sensitivity study of a dynamic thermodynamic sea ice model, *J. Geophys. Res.*, *98*, 2561–2586, doi:10.1029/92JC02015.
Holloway, G., et al. (2007), Water properties and circulation in Arctic Ocean models, *J. Geophys. Res.*, *112*, C04S03, doi:10.1029/2006JC003642.
Hu, H., and J. Wang (2010), Modeling effects of tidal and wave mixing on circulation and thermohaline structures in the Bering Sea: Process studies, *J. Geophys. Res.*, *115*, C01006, doi:10.1029/2008JC005175.
Hu, H., J. Wang, and D.-R. Wang (2011), A model-data study of the 1999 St. Lawrence Island polynya in the Bering Sea, *J. Geophys. Res.*, *116*, C12018, doi:10.1029/2011JC007309.
Ikeda, M. (1983), Linear instability of a current flowing along a bottom slope using a three-layer model, *J. Phys. Oceanogr.*, *13*, 208–223.
Ikeda, M., J. Wang, and A. Makshtas (2003), Importance of clouds to the decaying trend and decadal variability in the Arctic ice cover, *J. Meteorol. Soc. Jpn.*, *81*, 179–189.
Kantha, L. H., and C. A. Clayson (1994), An improved mixed layer model for geophysical applications, *J. Geophys. Res.*, *99*, 25,235–25,266.
König-Beatty, C., and D. M. Holland (2010), Modeling landfast sea ice by adding tensile strength, *J. Phys. Oceanogr.*, *40*(1), 185–198.
Kowalik, Z., and A. Proshutinsky (1994), *The Arctic Ocean tides, in The Polar Oceans and Their Role in Shaping the Global Environment: Nansen Centennial Volume in The Polar Oceans and Their Role in Shaping the Global Environment, Geophys. Monogr. Ser.*, *85*, edited by O. M. Johannessen, R. D. Muench and J. E. Overland, pp. 137–158, AGU, Washington, D. C., doi:10.1029/GM085p0137.
Long, Z., W. Perrie, C. L. Tang, E. Dunlap, and J. Wang (2012), Simulated interannual variations of freshwater content and sea surface height in the Beaufort Sea, *J. Clim.*, *25*, 1079–1095, doi:10.1175/2011JCI14121.1.
Mahoney, A., H. Eicken, A. G. Gaylord, and L. Shapiro (2007a), Alaska landfast sea ice: Links with bathymetry and atmospheric circulation, *J. Geophys. Res.*, *112*, C02001, doi:10.1029/2006JC003559.
Mahoney, A., H. Eicken, and L. Shapiro (2007b), How fast is landfast ice? A study of the attachment and detachment of nearshore ice at Barrow, Alaska, *Cold Reg. Sci. Technol.*, *47*, 233–255.
Manley, T. O., and K. Hunkins (1985), Mesoscale eddies of the Arctic Ocean, *J. Geophys. Res.*, *90*, 4911–4930.
Maslanik, J., S. Drobot, C. Fowler, W. Emery, and R. Barry (2007), On the Arctic climate paradox and the continuing role of atmospheric circulation in affecting sea ice conditions, *Geophys. Res. Lett.*, *34*, L03711, doi:10.1029/2006GL028269.
Maslanik, J., J. Stroeve, C. Fowler, and W. Emery (2011), Distribution and trends in Arctic sea ice age through spring 2011, *Geophys. Res. Lett.*, *38*, L13502, doi:10.1029/2011GL047735.
Mathis, J. T., R. S. Pickart, D. A. Hansell, D. Kadko, and N. R. Bates (2007), Eddy transport of organic carbon and nutrients from the Chukchi shelf into the deep Arctic basin, *J. Geophys. Res.*, *112*, C05011, doi:10.1029/2006JC003899.
Meier, H. E. M. (2002a), Regional ocean climate simulations with a 3D ice-ocean model for the Baltic Sea. Part 1: Model experiments and results for temperature and salinity, *Clim. Dyn.*, *19*, 237–253.
Meier, H. E. M. (2002b), Regional ocean climate simulations with a 3D ice-ocean model for the Baltic Sea. Part 2: Results for sea ice, *Clim. Dyn.*, *19*, 255–266.
Melling, H. (1993), The formation of a haline shelf front in wintertime in an ice-covered sea, *Cont. Shelf. Res.*, *13*, 1123–1147.
Mellor, G. L. (2004), *Users Guide for a 3-D, Primitive Equation, Numerical Ocean Model*, 39 pp., Atmos. and Oceanic Sci. Prog., Princeton Univ., Princeton, N. J.
Mellor, G. L., and L. Kantha (1989), An ice-ocean coupled model, *J. Geophys. Res.*, *94*, 10,937–10,954.
Mizobata, K., J. Wang, and S. Saitoh (2006), Eddy-induced cross-slope exchange maintaining summer high productivity of the Bering Sea shelf break, *J. Geophys. Res.*, *111*, C10017, doi:10.1029/2005JC003335.
Mizobata, K., S. Saitoh, and J. Wang (2008), Interannual variability of summer biochemical enhancement in relation to the mesoscale eddy at the shelf break in the vicinity of the Pribilof Islands, Bering Sea, *Deep Sea Res., Part II*, *55*, 1717–1728, doi:10.1016/j.dsr2.2008.03.002.
Mizobata, K., K. Shimada, R. Woodgate, S. Saitoh, and J. Wang (2010), Estimation of heat flux through the eastern Bering Strait, *J. Oceanogr.*, *66*(3), 405–424, doi:10.1007/s10872-010-0035-7.
Muench, R. D., J. T. Gunn, T. E. Whitledge, P. Schlosser, and W. Smethie (2002), An Arctic Ocean cold core eddy, *J. Geophys. Res.*, *105*, 23,997–24,006.
Nihoul, J. C. J., P. Adam, P. Brasseur, E. Deleersnijder, S. Djenidi, and J. Haus (1993), Three-dimensional general circulation model of the northern Bering Sea's summer ecohydrodynamics, *Cont. Shelf Res.*, *13*, 509–542.
Ohshima, K. I., and S. Nihashi (2005), A simple ice-ocean coupled model for the Antarctic ice melt season, *J. Phys. Oceanogr.*, *35*, 188–201.
Okkonen, S. R., C. J. Ashjian, R. G. Campbell, W. Maslowski, J. L. Clement-Kinney, and R. Potter (2009), Intrusion of warm Bering/Chukchi waters onto the shelf in the western Beaufort Sea, *J. Geophys. Res.*, *114*, C00A11, doi:10.1029/2008JC004870.
Pickart, R. S. (2004), Shelfbreak circulation in the Alaska Beaufort Sea: Mean structure and variability, *J. Geophys. Res.*, *109*, C04024, doi:10.1029/2003JC001912.
Pickart, R. S., T. J. Weingartner, L. J. Pratt, S. Zimmermann, and D. J. Torres (2009), Flow of winter-transformed Pacific water into the Western Arctic, *Deep Sea Res., Part II*, *52*(24–26), 3175–3198.
Proshutinsky, A., et al. (2001), Multinational effort studies differences among Arctic Ocean models, *Eos Trans. AGU*, *82*(51), 637–644.
Shimada, K., T. Kamoshida, M. Itoh, S. Nishino, E. Carmack, F. McLaughlin, S. Zimmermann, and A. Proshutinsky (2006), Pacific Ocean inflow: Influence on catastrophic reduction of sea ice cover in the Arctic Ocean, *Geophys. Res. Lett.*, *33*, L08605, doi:10.1029/2005GL025624.
Spall, M. A., R. S. Pickart, P. S. Fratantoni, and A. J. Plueddemann (2008), Western Arctic shelfbreak eddies: Formation and transport, *J. Phys. Oceanogr.*, *38*, 1644–1668, doi:10.1175/2007JPO3829.1.
Steele, M., R. Rebecca, and W. Ermold (2001), PHC: A global ocean hydrography with a high-quality Arctic Ocean, *J. Clim.*, *14*, 2079–2087.
Thorndike, A. S., and R. Colony (1982), Sea ice motion in response to the geostrophic winds, *J. Geophys. Res.*, *87*, 5845–5852, doi:10.1029/JC087iC08p05845.
Thorndike, A. S., D. A. Rothrock, G. A. Maykut, and R. Colony (1975), The thickness distribution of sea ice, *J. Geophys. Res.*, *80*, 4501–4513.
Wang, J., and M. Ikeda (1997), Diagnosing ocean unstable baroclinic waves and Meanders using quasi-geostrophic equations and Q-vector method, *J. Phys. Oceanogr.*, *27*(6), 1158–1172.
Wang, J., and M. Ikeda (2000), Arctic oscillation and Arctic sea-ice oscillation, *Geophys. Res. Lett.*, *27*, 1287–1290.
Wang, J., and M. Ikeda (2001), Arctic sea-ice oscillation: Regional and seasonal perspectives, *Ann. Glaciol.*, *33*, 481–492.
Wang, J., L. A. Mysak, and R. G. Ingram (1994), A numerical simulation of sea-ice cover in Hudson Bay, *J. Phys. Oceanogr.*, *24*, 2515–2533.
Wang, J., M. Jin, V. Patrick, J. Allen, D. Eslinger, C. Mooers, and T. Cooney (2001), Numerical simulation of the seasonal ocean circulation patterns and thermohaline structure of Prince William Sound, Alaska, *Fish. Oceanogr.*, *10*(Suppl. 1), 132–148.
Wang, J., Q. Liu, and M. Jin (2002), A user's guide for a Coupled Ice-Ocean Model (CIOM) in the Pan-Arctic and North Atlantic Oceans, *Tech. Rep. 02-01*, 65 pp., Int. Arctic Res. Cent.-Frontier Res. Syst. for Global Change, University of Alaska Fairbanks, Fairbanks, Alaska.

Wang, J., et al. (2003), Working towards improved small-scale sea ice and ocean modeling in the Arctic seas, *Eos Trans. AGU*, *84*(34), 325, 329–330.
Wang, J., Q. Liu, M. Jin, M. Ikeda, and F. J. Saucier (2005), A coupled ice-ocean model in the pan-Arctic and the northern North Atlantic Ocean: Simulation of seasonal cycles, *J. Oceanogr.*, *61*, 213–233.
Wang, J., K. Mizobata, H. Hu, M. Jin, S. Zhang, W. Johnson, and K. Shimada (2008), Modeling seasonal variations of ocean and sea ice circulation in the Beaufort and Chukchi Seas: A model-data fusion study, *Chin. J. Polar Sci.*, *19*(2), 168–184.
Wang, J., J. Zhang, E. Watanabe, K. Mizobata, M. Ikeda, J. E. Walsh, X. Bai, and B. Wu (2009a), Is the dipole anomaly a major driver to record lows in the Arctic sea ice extent?, *Geophys. Res. Lett.*, *36*, L05706, doi:10.1029/2008GL036706.
Wang, J., H. Hu, K. Mizobata, and S. Saitoh (2009b), Seasonal variations of sea ice and ocean circulation in the Bering Sea: A model-data fusion study, *J. Geophys. Res.*, *114*, C02011, doi:10.1029/2008JC004727.
Wang, J., K. Mizobata, M. Jin, and H. Hu (2009a), Sea Ice-Ocean-Oilspill Modeling System (SIOMS) for the Nearshore Beaufort and Chukchi seas: Parameterization and Improvement (Phase II), Final Report, OCS Study MMS 2008-021, 86 pp., Coastal Mar. Inst., Univ. of Alaska.
Wang, J., H. Hu, D. Schwab, G. Leshkevich, D. Beletsky, N. Hawley, and A. Clites (2010b), Development of the Great Lakes Ice-circulation Model (GLIM): Application to Lake Erie in 2003–2004, *J. Great Lakes Res.*, *36*, 425–436, doi:10.1016/j.jglr.2010.04.002.
Wang, J., H. Eicken, Y. Yu, X. Bai, H. Hu, K. Mizobata, J. Zhang, M. Ikeda, and J. Overland (2014), Abrupt Arctic changes and emerging ice-ocean processes in the Pacific Arctic Region and Bering Sea, in *The Pacific Arctic Region: Ecosystem Status and Trends in a Rapidly Changing Environment*, edited by J. M. Grebmeier and W. Maslowski, Springer, Heidelberg, N. Y.
Watanabe, E. (2011), Beaufort shelf break eddies and shelf-basin exchange of Pacific summer water in the western Arctic Ocean detected by satellite and modeling analyses, *J. Geophys. Res.*, *116*, C08034, doi:10.1029/2010JC006259.
Watanabe, E., J. Wang, T. Sumi, and H. Hasumi (2006), Arctic Dipole and its contribution to sea ice export from the Arctic in the last 20th century, *Geophys. Res. Lett.*, *33*, L23703, doi:10.1029/2006GL028112.
Weingartner, T. J., D. J. Cavalieri, K. Aagaard, and Y. Sasaki (1998), Circulation, dense water formation, and outflow on northeast Chukchi shelf, *J. Geophys. Res.*, *103*, 7647–7661.
Weingartner, T. J., K. Aagaard, R. Woodgate, S. Danielson, Y. Sasaki, and D. J. Cavalieri (2005), Circulation on the north central Chukchi Sea shelf, *Deep Sea Res., Part II*, 3150–3174.
Winsor, P., and D. Chapman (2004), Pathways of Pacific water across the Chukchi Sea: A numerical model study, *J. Geophys. Res.*, *109*, C03002, doi:10.1029/2003JC001962.
Woodgate, R., T. J. Weingartner, and K. Aagaard (2005), A year in the physical oceanography of the Chukchi Sea: Moored measurements from autumn 1990–1991, *Deep Sea Res., Part II*, 3116–3149.
Woodgate, R. A., T. Weingartner, and R. Lindsay (2010), The 2007 Bering Strait oceanic heat flux and anomalous Arctic sea-ice retreat, *Geophys. Res. Lett.*, *37*, L01602, doi:10.1029/2009GL041621.
Wu, B., J. Wang, and J. E. Walsh (2006), Dipole anomaly in the winter Arctic atmosphere and its association with Arctic sea ice motion, *J. Clim.*, *19*(2), 210–225, doi:10.1175/JCLI3619.1.
Yang, J. (2006), The seasonal variability of the Arctic Ocean Ekman transport and its role in the mixed layer heat and salt fluxes, *J. Clim.*, *19*, 5366–5387, doi:10.1175/JCLI3892.1.
Yao, T., C. L. Tang, and I. K. Peterson (2000), Modeling the seasonal variation of sea ice in the Labrador Sea with a coupled multi-category ice model and the Princeton Ocean Model, *J. Geophys. Res.*, *105*, 1153–1165.
Yu, Y., H. Stern, C. Fowler, F. Fetterer, and J. Maslinik (2013), Interannual variability of Arctic landfast ice between 1976–2007, *J. Clim.*, *27*, 227–243, doi:10.1175/JCLI-D-13-00178.1.
Zhang, J., R. Woodgate, and R. Moritz (2010), Sea ice response to atmospheric and oceanic forcing in the Bering Sea, *J. Phys. Oceanogr.*, *40*(8), 1729–1747, doi:10.1175/2010JPO4323.1.